Density Functional Calculations of Electronic Structure, Charge Distribution, and Spin Coupling in Manganese−Oxo Dimer Complexes

X. G. Zhao, W. H. Richardson, J.-L. Chen,† J. Li, and L. Noodleman*

Department of Molecular Biology, TPC15, The Scripps Research Institute, La Jolla, California 92037

H.-L. Tsai‡ and D. N. Hendrickson

Department of Chemistry, University of California, San Diego, La Jolla, California 92093

Received November 2, 1995⊗

We have calculated the electronic structures of five different manganese−oxo dimer complexes using density functional methods combined with the broken symmetry and spin projection concepts. The number of carboxylate, oxo, and peroxo bridging ligands was varied, and the terminal ligands were triazacyclononane (TACN). The formal Mn oxidation states varied from Mn^{III}_2 and $Mn^{III}Mn^{IV}$ to Mn^{IV}_2. These complexes have been synthesized and their X-ray structures and magnetic properties measured previously. We have calculated the Heisenberg spin coupling parameters J and resonance delocalization parameters B for all of these systems. Despite the very small energy differences involved, there is a good correspondence between calculated and experimental Heisenberg J parameters. We have analyzed potential changes in the calculated effective Heisenberg coupling J_{eff} for the mixed-valence $Mn^{III}Mn^{IV}$ complexes when partial or complete delocalization due to the B parameter is taken into account. These changes depend also on the energy of the relevant intervalence band. Surprisingly, in the two mixed-valence systems studied, the high spin $S = {}^5/_2$ state lies below $S = {}^7/_2$. This is consistent with spin coupling between Mn with site spins $S_1 = 1$, $S_2 = {}^3/_2$, corresponding to intermediate spin Mn(I) and Mn(II) respectively, instead of the coupling expected from the formal oxidation states, $S_1 = 2$, $S_2 = {}^3/_2$ from high spin Mn(III) and Mn(IV). The spin and charge distributions in the broken symmetry ground states are also consistent with intermediate spin $S_1 = 1$, $S_2 = {}^3/_2$. The calculated charge distributions show strong metal−ligand covalency. In fact, as the formal oxidation states of the Mn sites increase, the net Mn charges generally show a slow decrease, consistent with a very strong ligand → metal charge transfer, particularly from μ-oxo or μ-peroxo ligands. TACN is a better donor ligand than carboxylate, even when calculated on a per donor atom basis. The ligand atom charge transfer order is peroxo ≥ oxo ≫ TACN > acetate. The TACN > acetate ordering is expected from the spectrochemical series, but the strong charge transfer and strong metal−ligand covalency of peroxo and oxo ligands with the Mn sites cannot be simply related to their positions in the spectrochemical series. In the $Mn^{IV}_2(\mu\text{-}O)_2(\mu\text{-}O_2)(TACN)_2$, each peroxo oxygen has a small charge (−0.3), much less than found for each μ-O atom (−0.7). The high-spin $S = 3$ state lies quite low in energy, 8 kcal/mol from our calculations and about 4 kcal/mol based on the experimental Heisenberg spin coupling parameters. Potential molecular oxygen dissociation pathways involving a spin $S = 1$ state are discussed. Effective ligand field diagrams are constructed from the calculated energy levels which display the competition between spin polarization splitting and the ligand field t_{2g}−e_g splitting and allow comparisons of electronic structure among different complexes. The electronic structure and spin coupling of these complexes was also compared to the corresponding "core-only" complexes where both TACN ligands were removed, yielding a far weaker ligand field. There is a strong ferromagnetic shift in the "core-only" complexes compared with the complete TACN complexes, also showing the effects of a weaker ligand field.

1. Introduction

Mn−oxo dimer complexes appear as subunits in a number of biologically important metalloenzymes, in particular in the water oxidation complex (WOC) of photosystem II,[1−3] in pseudocatalase,[4] and in the manganese form of ribonucleotide reductase.[5,6] The last two systems contain dinuclear Mn sites,[4] while the WOC is almost certainly tetranuclear.[3] All three of these quite different enzymes catalyze processes involving multiple electron and proton transfer events, and all have related coordination geometries. Below, we will focus on the connection of model systems to the biologically important and catalytically novel WOC. While the basic set of steps involved in its catalytic mechanism have been established, many critical questions remain unresolved.

The WOC operates by the light-driven four-electron oxidation of two water molecules to molecular oxygen with stepwise oxidation of the cluster from state S_0 to S_4.[2,7,8] In this process, the four electrons and four protons are made available for the

† Present address: Synchrotron Research Center, Hsin Chu, Taiwan, ROC.

‡ Present address: Department of Chemistry, National Cheng Kung University, Tainan, Taiwan, ROC.

⊗ Abstract published in *Advance ACS Abstracts,* February 15, 1997.

(1) Wieghardt, K. *Angew. Chem., Int. Ed. Engl.* **1989**, *28*, 1153−1172.
(2) Sauer, K. *Acc. Chem. Res.* **1980**, *13*, 249−256.
(3) Brudvig, G. W.; Thorp, H. H.; Crabtree, R. H. *Acc. Chem. Res.* **1991**, *24*, 311−316.
(4) Gamelin, D. R.; Kirk, M. L.; Stemmler, T. L.; Pal, S.; Armstrong, W. H.; Penner-Hahn, J. E.; Solomon, E. I. *J. Am. Chem. Soc.* **1994**, *116*, 2392−2399.
(5) Willing, A.; Follmann, H.; Auling, G. *Eur. J. Biochem.* **1988**, *170*, 603−611.
(6) Willing, A.; Follmann, H.; Auling, G. *Eur. J. Biochem.* **1988**, *175*, 167−173.

S0020-1669(95)01430-3 CCC: $14.00

process of photosynthesis. The overall process usually[9,10] requires the cooperation of two different photosystems (I and II), and a number of carriers for electrons and protons, with coupling to biosynthesis and ATP generation.[7,8,11] In the WOC, upon successive one-electron oxidation steps, the Mn site oxidation states increase, finally transferring electrons from bound water or hydroxyl ligands to the Mn cluster and releasing O_2 in the S_4 to S_0 transition. This step occurs spontaneously, once the $S_3 \rightarrow S_4$ transition is achieved. While in a number of models it has been proposed that both waters (or hydroxyls) are bound to the Mn cluster prior to O_2 release,[3] with intermediates including bound oxo or peroxo groups, there are experimental results that are very compatible with alternative mechanisms. Messinger's[12] recent experiments with $H_2{}^{18}O$ exchange imply that there is only one slowly exchanging substrate water molecule in the S_3 state of PS II. This is consistent with only one substrate water bound to the cluster. The other faster exchanging water may be more loosely coordinated to a different non-manganese site which could be a protein residue or possibly Ca^{2+}. Alternatively, the second water molecule may only bind to the cluster in the final S_4 state.

The high oxidation state Mn sites compete with bound protons for the electron density, and while the cluster is oxidized in successive steps, protons are also released from the associated waters (or hydroxyls).[13] These protons may be transferred to basic groups on nearby amino acid residues, particularly the close lying redox active tyrosine Y_Z.[14] These basic groups or perhaps others in a proton transport chain release protons at various stages into the luminal space of the thylakoid membrane.

There are a number of mysteries in the mode of operation of the WOC complex. The manganese tetramer stays at more negative redox potential than the $Tyr^{\bullet}/Tyr^{-}$ couple (or neutral Tyr after protonation)[13,14] through several one-electron oxidation steps (four such steps).[11] The detailed energetics of this process are not well understood, but some factors should facilitate this: (1) high oxidation state Mn ions will acidify bound water protons; (2) proton removal from the cluster is made easier by the nearby bases;[13,14] (3) the polynuclear manganese cluster electronic structure should display extensive metal−ligand covalency (by analogy to the related synthetic Mn complexes analyzed in the present work).

The tyrosine (probably with the donor in the neutral non-radical form)[14] in turn provides the electron to the oxidized chromophore P680 where the initial electron transfer event induced by photosystem II light absorption occurs. One or two water molecules are bound by the cluster and both are oxidized, but at which steps of the cluster oxidation this occurs, and what ligands (if any) they replace is not known. Spectroscopic probes give only some indications of the changes that occur during the several oxidation steps.[15−17] How the protein/solvent/membrane environment modulates the electronic structure/reactivity of the active site cluster is not known. The detailed energetics of how shifts in electron density upon oxidation are correlated with increasing acidity of the bound protons and the energetics of the final release of O_2 in the triplet spin state need to be resolved. Further, one may ask whether the presence of a spin-coupled transition metal complex is essential to the reaction, and what role is played by four coupled Mn sites compared with 2Mn or a single Mn. (For some current mechanistic proposals, see Proserpio et al.[18]) Further issues include the extent of metal−ligand covalency and valence delocalization between manganese sites and whether these play an important role in the rate or energetics of charge separation.

Throughout the process of electron and proton removal from the cluster, reactive oxygen intermediates including peroxide O_2^{2-}, or possibly superoxide $O_2^{-\bullet}$ must remain bound to the Mn complex to avoid toxicity. Four oxidizing equivalents (holes) must be stored in the Mn_4 complex without undesirable oxidations of substrate or bound amino acid side chains.[13] Britt[14] and Nugent[19] have shown that the ligand radical center observed by electron paramagnetic resonance (EPR) in the Ca depleted "S_3" state and originally assigned to a histidine radical[8,20] is instead the nearby tyrosine ($Y_{Z^{\bullet}}$ radical), broadened by coupling to the paramagnetic Mn cluster, with the internal Mn cluster oxidation state either S_3 or S_2.

Currently, the coordination geometry of the WOC complex is not known, although butterfly, dimer-of-dimers, and cubane structures have been postulated based on X-ray absorption fine structure (EXAFS) or EPR hyperfine data.[1,21] The EXAFS data[16] implicates Mn−Mn distances of 2.7 Å (probably two Mn−Mn distances of this type) and 3.2 Å (probably one distance of this type) within the 4Mn cluster of the WOC (in the S_2 oxidation state).[8] From distances in related synthetic analogues, these would be consistent with $Mn_2(\mu\text{-}O)_2(\mu\text{-}OAc)_1$ core[22] for the shorter Mn−Mn distance and a $Mn_2(\mu\text{-}O)_1(\mu\text{-}OAc)_2$ core for longer Mn−Mn distances.[23,24] The $Mn_2(\mu\text{-}O)_2(\mu\text{-}O_2)$[25] structure may also be quite relevant to the WOC since the O═O bond formation ending in molecular oxygen must go through some intermediate stages, and a peroxo type intermediate is quite possible, but the binding mode need not be the same as that found in the synthetic system. The carboxylate bridges arise from glutamate or aspartate, and terminal ligands to the cluster are presumably also some combination of Asp, Glu, and histidine (His) based on EXAFS, electron-nuclear-double-resonance (ENDOR), and electron-spin-echo-modulation (ESEEM) spectroscopies.[8,16,26] This EXAFS (and XANES) data was obtained mainly for the S_2 oxidation state of the five-state WOC photocycle. X-ray absorption near edge (XANES) data[27]

(7) Rutherford, A. W.; Boussac, A.; Zimmerman, J.-L. *New J. Chem.* **1991**, *15*, 491−500.
(8) Wieghardt, K. *Angew. Chem., Int. Ed. Engl.* **1994**, *33*, 725−728.
(9) Barber, J. *Nature* **1995**, *376*, 388−389.
(10) Greenbaum, E.; Lee, J. W.; Tevault, C. V.; Blankenship, S. L.; Mets, L. J. *Nature* **1995**, *376*, 438−441.
(11) Kaim, W.; Schwederski, B. *Bioinorganic Chemistry: Inorganic Elements in the Chemistry of Life*; Wiley: Chichester, England, 1994.
(12) Messinger, J.; Badger, M.; Wydrzynski, T. *Proc. Natl. Acad. Sci. U.S.A.* **1995**, *92*, 3209−3213.
(13) Babcock, G. T.; Barry, B. A.; Debus, R. J.; Hoganson, C. W.; Atamian, M.; McIntosh, L.; Sithole, I.; Yocum, C. F. *Biochemistry* **1989**, *28*, 9557−9565.
(14) Gilchrist, M. L., Jr.; Ball, J. A.; Randall, D. W.; Britt, R. D. *Proc. Natl. Acad. Sci. U.S.A.* **1995**, *92*, 9545−9549.
(15) Sivaraja, M.; Philo, J. S.; Lary, J.; Dismukes, G. C. *J. Am. Chem. Soc.* **1989**, *111*, 3221.
(16) DeRose, V. J.; Mukerji, I.; Latimer, M. J.; Yachandra, V. K.; Sauer, K.; Klein, M. P. *J. Am. Chem. Soc.* **1994**, *116*, 5239−5249.
(17) Kim, D. H.; Britt, R. D.; Klein, M. P.; Sauer, K. *J. Am. Chem. Soc.* **1990**, *112*, 9389.
(18) Proserpio, D. M.; Hoffmann, R.; Dismukes, G. C. *J. Am. Chem. Soc.* **1992**, *114*, 4374−4382.
(19) Hallahan, B. J.; Nugent, J. H. A.; Warden, J. T.; Evans, M. C. W. *Biochemistry* **1992**, *31*, 4562−4573.
(20) Boussac, A.; Zimmermann, J. L.; Rutherford, A. W.; Lavergne, J. *Nature* **1990**, *347*, 303−306.
(21) Christou, G. *Acc. Chem. Res.* **1989**, *22*, 328−335.
(22) Wieghardt, K.; Bossek, U.; Zsolnai, L.; Huttner, G.; Blondin, G.; Girerd, J.-J.; Babonneau, F. *J. Chem. Soc., Chem. Commun.* **1987**, 651.
(23) Wieghardt, K.; Bossek, U.; Ventur, D.; Weiss, J. *J. Chem. Soc., Chem. Commun.* **1985**, 347.
(24) Wieghardt, K.; Bossek, U.; Bonvoisin, J.; Beauvillain, P.; Girerd, J. J.; Nuber, B.; Weiss, J.; Heinze, J. *Angew. Chem., Int. Ed. Engl.* **1986**, *25*, 1030−1031.
(25) Bossek, U.; Weyhermuller, T.; Wieghardt, K.; Nuber, B.; Weiss, J. *J. Am. Chem. Soc.* **1990**, *112*, 6387−6388.
(26) DeRose, V. J.; Yachandra, V. K.; McDermott, A. E.; Britt, R. D.; Sauer, K.; Klein, M. P. *Biochemistry* **1991**, *30*, 1335−1341.

for the Mn K-edge energy over the five-state cycle driven by flashing light shows that the K-edge energy shifts up by 1.2 eV after the $S_2 \rightarrow S_3$ transition, which is most simply interpreted as a one-electron oxidation of the Mn cluster. However, partial oxidation of a ligand to the Mn cluster cannot be excluded. Integer spin EPR data indicates a total spin $S_t = 1$ is consistent with the spectrum for the one-electron more reduced state called S_1.[28,29] (Under different conditions of dark adaptation, Brudvig et al.[30] find that the S_1 oxidation state displays a diamagnetic $S_t = 0$ spin state based on dipolar spin−lattice relaxation measurements for the stable tyrosine radical Y_D.) Extensive EPR investigations of the S_2 state show the presence of an $S_t = {}^1/_2$ state showing a multiline (19-line) EPR signal due to Mn hyperfine interactions.[17,31] Under certain conditions the S_2 oxidation state also displays a broad signal with a g value near 4.1, indicative of total spin $S_t = {}^3/_2$ or $S_t = {}^5/_2$.[17,32] Further, the $g = 4$ signal also shows a multiline pattern in PSII membranes treated with NH_4Cl, indicating the likelihood of a tetranuclear Mn cluster. For the S_2 state, the expected Mn site oxidation states are either $Mn^{III}{}_3Mn^{IV}$ or $Mn^{IV}{}_3Mn^{III}$ as required to be consistent with the half-integer spin states observed. In either case, mixed-valence $Mn^{III}Mn^{IV}$ pair interactions are quite relevant.

While it now appears clear that the WOC contains a tetranuclear ($Mn_4O_xOAc_y$) center, some major issues of electronic structure and chemical bonding in the WOC and related systems can be assessed based on dimeric Mn complexes. A number of synthetic dimer complexes with manganese−oxo−carboxylato centers have now been synthesized and structurally characterized by X-ray diffraction.[1,4,33−37] Among the complexes with terminal nitrogen donor ligands, those with *sym*-triazacyclononane (TACN) ligands form a structurally well-defined series with variations in Mn oxidation states, and in the number of oxo, peroxo, and carboxylate bridges.[1,23−25]

Magnetic susceptibility measurements have been made on a number of these complexes, and fit to a Heisenberg spin-coupling model.[1,23−25] There are also additional data on redox potentials, pK_a's, and optical spectra in some cases.[1,24,38]

The bonding of high oxidation state manganese to oxo ligands is complicated by any standard. Strong bonds are formed between the formally Mn(III) or Mn(IV) ions and the μ-*O* ligands. At the same time individual Mn sites retain a high-spin configuration (or intermediate spin) with less than a half-filled d-shell, and there is significant spin-coupling, either ferromagnetic or antiferromagnetic, between adjacent Mn sites via the oxo or carboxylato bridges.

A full understanding of these issues will clearly require a concerted view utilizing several techniques. From a theoretical viewpoint, a first step would be to understand the electronic structure and energetics of the $LMn(O)_x(OAc)_yMnL$-bridged system. In this paper, we will focus on two related goals. The first is to calculate the Heisenberg spin coupling parameters for well-defined Mn−oxo dimer complexes where structures are known and corresponding magnetic susceptibilities have been measured. The second goal is to understand various aspects of electronic structure in these systems. This goal entails understanding the nature and origin of shifts in charge and spin density in related systems and comparisons to formal oxidation state models. Further, the calculated and experimental magnetic coupling Heisenberg parameters will be related to the effective ligand fields, spin polarization, and oxidation states at the Mn ions. To compare different complexes, an effective ligand field model is devised and used as a guide in addition to the detailed orbital electronic structure. The magnetic and electronic properties of the complete complexes will also be compared with "core-only" complexes where the TACN ligands have been removed. This both weakens the ligand field at the Mn ions and removes significant electron donation by the tridentate TACN nitrogens. This provides a stepping stone toward understanding more complicated ligand substitution effects.

We will examine trends among five different complexes and compare properties, especially Heisenberg spin coupling J and resonance delocalization (double exchange) B parameters. The Heisenberg coupling parameters can be compared with those observed experimentally. These variations will be examined as a function of the number of oxo and carboxylate bridges, and as a function of Mn oxidation state (mixed-valence Mn(III)−Mn(IV) vs Mn(III)−Mn(III) and Mn(IV)−Mn(IV)).

2. Methodology

2.1. Nonlocal Density Functional Calculations. All calculations used the Amsterdam Density Functional programs developed by te Velde, Baerends, and co-workers,[39] program version AMOL (Aug 1992),[40] but with basis sets from the later ADF codes, version, 1.0.1 (July, 1993).[41] Calculations on complexes **4** and **5** used the more recent ADF 1.1.3 (Nov 1994) code, but with the same basis sets, for consistency. Calculations were of fully nonlocal self-consistent-field type and utilized the local exchange-correlation potential of Vosko−Wilk−Nusair (VWN).[42] The nonlocal exchange and correlation energy terms and corresponding potentials are due to Becke and Perdew,[43−46] respectively. Then the overall exchange-correlation potential is called VBP. All molecular calculations were spin unrestricted, so as to allow for substantial spin polarization on metal and ligand sites. The bonding energies were calculated with respect to a reference state composed of spin-restricted atoms making up the molecule. Identical grids are used for the molecule and the restricted atom fragments in the energy difference evaluation.[39,47,48] These methods are a development of the earlier Ziegler−Rauk transition state method,[49] allowing an accurate calculation of the molecular binding energy with respect to the spin

(27) Ono, T.; Noguchi, T.; Inoue, Y.; Kusunoki, M.; Matsushita, T.; Oyanagi, H. *Science* **1992**, *258*, 1335−1337.
(28) Dexheimer, S. L.; Klein, M. P. *J. Am. Chem. Soc.* **1992**, *114*, 2821−2826.
(29) Kirk, M. L.; Chan, M. K.; Armstrong, W. H.; Solomon, E. I. *J. Am. Chem. Soc.* **1992**, *114*, 10432.
(30) Koulougliotis, D.; Hirsh, D. J.; Brudvig, G. W. *J. Am. Chem. Soc.* **1992**, *114*, 8322−8323.
(31) Dismukes, G. C.; Siderer, Y. *Proc. Natl. Acad. Sci. U.S.A.* **1981**, *78*, 274.
(32) Haddy, A.; Dunham, W. R.; Sands, R. H.; Aasa, R. *Biochem. Biophys. Acta* **1992**, *1099*, 25−34.
(33) Pal, S.; Olmstead, M. M.; Armstrong, W. H. *Inorg. Chem.* **1995**, *34*, 4708−4715.
(34) Pessiki, P. J.; Dismukes, G. C. *J. Am. Chem. Soc.* **1994**, *116*, 898−903.
(35) Pessiki, P. J.; Khangulov, S. V.; Ho, D. M.; Dismukes, G. C. *J. Am. Chem. Soc.* **1994**, *116*, 891−897.
(36) Vincent, J. B.; Tsai, H.-L.; Blackman, A. G.; Wang, S.; Boyd, P. D. W.; Folting, K.; Huffman, J. C.; Lobovsky, E. B.; Hendrickson, D. N.; Christou, G. *J. Am. Chem. Soc.* **1993**, *115*, 12353−12361.
(37) Oberhausen, K. J.; O'Brien, R. J.; Richardson, J. F.; Costa, R.; Latour, J.-M.; Tsai, H.-L.; Hendrickson, D. N. *Inorg. Chem.* **1993**, *32*, 4561−4565.
(38) Wieghardt, K.; Bossek, U.; Nuber, B.; Weiss, J.; Bonvoisin, J.; Corbella, M.; Vitols, S. E.; Girerd, J. J. *J. Am. Chem. Soc.* **1988**, *110*, 7398−7411.
(39) te Velde, G.; Baerends, E. J. *J. Comp. Phys.* **1992**, *99*, 84−98.
(40) AMOL. Department of Theoretical Chemistry, Vrije Universiteit, Amsterdam, Aug 1992.
(41) ADF codes version 1.0.1. Department of Theoretical Chemistry, Vrije Universiteit, Amsterdam, July 1993.
(42) Vosko, S. H.; Wilk, L.l; Nusair, M. *Can. J. Phys.* **1980**, *58*, 1200−1211.
(43) Becke, A. D. In *The Challenge of d and f Electrons*; Salahub, D. R., Zerner, M. C., Eds.; American Chemical Society: Washington, DC, 1989; pp 165−179.
(44) Becke, A. D. *J. Chem. Phys.* **1986**, *84*, 4524−4529.
(45) Perdew, J. P. *Phys. Rev. B* **1986**, *33*, 8822−8824.
(46) Perdew, J. P. *Phys. Rev. B* **1986**, *34*, 7406.
(47) Boerrigter, P. M.; te Velde, G.; Baerends, E. J. *Int. J. Quantum Chem.* **1988**, *33*, 87−113.

restricted atom reference state. The reference state subtracts out when energy differences between different spin states are evaluated. Matrix elements appearing in the matrix eigenvalue equation are computed using a cellular integration method, with special rules within atomic spheres and Gauss product rules for the interstitial region, as developed by te Velde, Beorrigter, and Baerends.[47] The accuracy parameter for the numerical integration grid used was ACCINT = 3.5. Convergence is obtained when the change in the mean of the diagonal elements of the density matrix (called the ADP) is less than 0.0003 in AMOL (the default convergence criteria). In ADF 1.1.3, the convergence criteria used was that the maximum element of the commutator of the Fock and the *P* matrix (density matrix) fall below 3×10^{-5}, and that the norm of the commutator matrix also fall below 3×10^{-4} (also the default criteria). All calculations were made either on a cluster of HP 9000/735 workstations or on the HP/Convex SPP computer at Scripps.

2.2. Basis Sets. The basis sets used were of Slater triple-ζ type including also one set of polarization functions per atom type. We used basis set IV from the ADF codes version 1.0.1 (July 1993).[41] In particular, the Mn atom had triple-ζ 3d and 4s basis sets plus one 4p polarization function. Carbon, oxygen, and nitrogen had triple-ζ 2s,2p plus one 3d polarization function, and hydrogen triple-ζ 1s plus one 2p polarization. Core orbitals were frozen through Mn(3s,3p) and C,N,O(1s). For the charge density fitting, the standard auxiliary charge density fit sets were used. The actual orbital, core, and charge density sets used are included in supplementary material.

2.3. Electrostatic Potential (ESP) Charge Calculations. The standard AMOL[40] and ADF 1.1.3 computer programs provide an analysis of the overall charge and spin distributions using a Mulliken population analysis. The molecular orbitals are similarly analyzed with a Mulliken population analysis based on the atomic symmetrized fragment orbitals. We also sought a method of analyzing the charge distribution based on a specific physical property, the molecular electrostatic potential (MEP) outside the envelope of atomic spheres with appropriate van der Waals radii. We modified the CHELPG code of Breneman and Wiberg[50] to treat molecular symmetry carefully, symmetrically centering the box in which the grid of points is constructed, and using singular value decomposition[51] in place of the standard Gauss−Jordan matrix inversion. The grid used in the fit extended from the various van der Waals spheres to an outer atomic sphere of 5 Å for each atom, and with a grid spacing of 0.2 Å. The van der Waals atomic radii chosen were: 1.5, 1.4, 1.7, 1.55, and 1.2 Å for Mn, O, C, N, and H, respectively. The values for C, N, and H were proposed by Bondi,[52] while for oxygen we have used the smaller radius (1.4 Å) proposed by Tunon et al.[53] The Mn van der Waals radius was set as 1.5 Å, intermediate between those of Ni and Zn.[52] In previous work, we also used 1.5 Å for the radius of Fe.[54] The MEP was fit using a least-squares procedure to a set of point charges centered at the atomic nuclei which generate a best fit potential. The fit included constraint equations for conservation of total charge and for the correct dipole moment vector determined from the AMOL density.[54,55] Singular value decomposition (SVD) analysis was used to minimize sensitivity of the charges to noise in the target electrostatic potential.[51] Details of this methodology and applications to transition metal and organic systems is discussed in detail in recent papers.[54,55]

2.4. Geometric Issues. The five complexes studied in the present work are as follows: **1**, $[Mn^{III}_2(\mu\text{-O})(OAc)_2(TACN)_2]^{2+}$;[56] **2**, $[Mn^{III}Mn^{IV}(\mu\text{-O})(OAc)_2(TACN)_2]^{3+}$;[24] **3**, $[Mn^{III}Mn^{IV}(\mu\text{-O})_2(OAc)(TACN)_2]^{2+}$,[22] **4**, $Mn^{IV}_2(\mu\text{-O})_2(\mu\text{-O}_2^{2-})(TACN)_2]^{2+}$;[25] **5**, $Mn^{IV}_2O_3(TACN)_2]^{2+}$.[38] The core-only analogues, omitting the two terminal (TACN) ligands, were also studied, in the same geometries as in the respective complete complexes. The syntheses, X-ray structures, and magnetic properties of complexes **1**−**5** have been reported in the literature. The calculations we have made are on the cationic Mn dimer complexes and do not include the counterions. The crystal structure of the Mn dimer complexes were appropriately averaged to obtain C_s molecular symmetry; this typically required only small changes in bond lengths and angles. For complex **2**, $Mn^{III}Mn^{IV}(\mu\text{-O})(OAc)_2(TACN)_2$, however, there are larger deviations from the idealized C_s symmetry. These involve in particular the Mn−O bond lengths to the carboxylates, which differ by 0.05 Å. This difference between the idealized and X-ray geometries has potential physical consequences, which will be examined later. Geometries used for the calculations were derived from experimental Mn−oxo−carboxylate TACN complexes. The molecules were oriented so that the mirror plane was always the *xy* plane, with *z* perpendicular to this, and so that the Mn atoms lie on ±*x*. Important bond lengths and angles used in the calculations are summarized in Table 1. Cartesian coordinates for all calculations are provided as Supporting Information. Distances and angles within the manganese−oxo−carboxylato core, and bond lengths and angles to the nitrogens of the TACN ligands were taken directly from the experimental X-ray structures. Where the experimental ligand was (*N*-methyl)$_3$−TACN), unsubstituted TACN was used as the model. Tables 2 and 3 summarize the differences between our idealized C_s symmetries for complexes **2** and **3** and the X-ray structures for the core region and for the Mn−N bonds. The deviations for complex **2** are seen to be larger than those for complex **3**. Next, we consider the geometries of the TACN ligands. Initially, our plan was to use the complete experimental geometries of the TACN's in the original complexes; however, we found that in various complexes, the experimental C−C and C−N single bonds of the TACN were quite short, 0.1 Å or more shorter than expected for C−C and C−N single bonds. Evidently, in some of these complexes, the TACN ligands are fluxional, and it has proven difficult to determine proper C−C and C−N bond lengths. This is confirmed by the structural map in Weighardt et al.[38] (see their Figure 6) which shows very large thermal ellipsoids on the carbons of the TACN ligands. We therefore used the TACN geometry for the heavy atoms of the $Mn^{III}_2(OAc)_2O(TACN)_2$ complex, where typical C−C and C−N single bond lengths were observed (C−C = 1.52, 1.52, and 1.54 Å and C−N = 1.49, 1.49, and 1.50 Å). The H positions were determined first by molecular modeling (with starting values, N−H = 0.97 Å and C−H = 1.09 Å) and subsequently by calculating optimized bond lengths, angles, and dihedral angles associated with the H positions for the free TACN ligand using geometry optimization from the latest ADF codes (ADF 1.1.3)[57]

Table 1. Bond Lengths and Angles of Mn Ions with Ligands

	complexes				
	1	**2**	**3**	**4**	**5**
	Bond Lengths, Å				
Mn···Mn′	3.09	3.23	2.59	2.53	2.30
Mn−$O_{\mu\text{-in}}$	1.79	1.83			1.82
Mn′−$O_{\mu\text{-in}}$	1.79	1.81			1.83
Mn−$O_{\mu\text{-out}}$			1.81	1.81	1.82
Mn′−$O_{\mu\text{-out}}$			1.81	1.81	1.82
Mn−O_{ac}	2.06	1.97	2.08		
Mn′-$O_{ac'}$	2.06	1.97	2.08		
Mn−O_p				1.83	
Mn′−$O_{p'}$				1.83	
Mn−N_{out}	2.19	2.11	2.13	2.09	2.12
Mn−N_{in}	2.07	2.13	2.11	2.11	2.11
Mn′−$N_{out'}$	2.19	2.11	2.13	2.10	2.12
Mn′−$N_{in'}$	2.07	2.12	2.11	2.12	2.09
O_p−$O_{p'}$				1.46	
	Bond Angles, deg				
Mn−$O_{\mu\text{-in}}$−Mn′	119.8	125.0			78.0
Mn−$O_{\mu\text{-out}}$−Mn′			91.1	88.6	78.2

(48) te Velde, G. Numerical Integration and Other Methodological Aspects of Band Structure Calculations. Ph.D. Thesis, Vrije University (1990).
(49) Ziegler, T.; Rauk, A. *Theor. Chim. Acta* **1977**, *46*, 1−10.
(50) Breneman, C. M.; Wiberg, K. B. *J. Comput. Chem.* **1990**, *11*, 361−373.
(51) Press, W. H.; Flannery, B. P.; Teukolsky, S. A.; Vetterling, W. T. *Numerical Recipes. The Art of Scientific Computing*, Cambridge University Press: Cambridge, U.K., 1986.
(52) Bondi, A. *J. Chem. Phys.* **1964**, *64*, 441.
(53) Tuñón, I.; Silla, E.; Pascual-Ahuir, J.-L. *J. Am. Chem. Soc.* **1993**, *115*, 2226−2230.
(54) Mouesca, J.-M.; Chen, J. L.; Noodleman, L.; Bashford, D.; Case, D. A. *J. Am. Chem. Soc.* **1994**, *116*, 11898−11914.
(55) Chen, J. L.; Noodleman, L.; Case, D. A.; Bashford, D. *J. Phys. Chem.* **1994**, *98*, 11059−11068.
(56) Bossek, U.; Wieghardt, K.; Nuber, B.; Weiss, J. *Inorg. Chim. Acta* **1989**, *165*, 123−129.
(57) ADF codes version 1.1.3. Department of Theoretical Chemistry, Vrije Universiteit, Amsterdam Nov 1994.

Table 2.

A. Geometry of $[Mn^{III}Mn^{IV}O(Oac)_2(tacn)_2]^{3+}$

experimental geometry[a]		input geometry[b,c]	
	Distances, Å		
$Mn_1\cdots Mn_2$	3.230(0)	$Mn\cdots Mn'$	3.23
Mn_1-O_1	1.826(6)	$Mn-O_\mu$	1.83
Mn_1-O_2	1.948(6)	$Mn-O_{ac}$	1.97
Mn_1-O_4	1.999(6)	$Mn-O_{ac1}$	1.97
Mn_1-N_1	2.089(8)	$Mn-N_{out}$	2.11
Mn_1-N_2	2.133(8)	$Mn-N_{in}$	2.13
Mn_1-N_3	2.141(8)	$Mn-N_{out1}$	2.11
Mn_2-O_1	1.814(6)	$Mn'-O_\mu$	1.81
Mn_2-O_3	2.000(5)	$Mn'-O_{ac'}$	1.97
Mn_2-O_5	1.951(7)	$Mn'-O_{ac1'}$	1.97
Mn_2-N_4	2.131(6)	$Mn'-N_{out'}$	2.11
Mn_2-N_5	2.117(8)	$Mn'-N_{in'}$	2.12
Mn_2-N_6	2.099(9)	$Mn'-N_{out1'}$	2.11
	Angles, deg		
$Mn_1-O_1-Mn_2$	125.1(3)	$Mn-O_\mu-Mn'$	125.04
$O_1-Mn_1-N_1$	97.0(3)	$O_\mu-Mn-N_{out}$	98.23
$O_1-Mn_1-N_3$	99.5(3)	$O_\mu-Mn-N_{out1}$	98.23
$O_1-Mn_1-N_2$	178.3(3)	$O_\mu-Mn-N_{in}$	179.74
$O_1-Mn_1-O_2$	93.5(3)	$O_\mu-Mn-O_{ac}$	93.30
$O_1-Mn_1-O_4$	93.2(3)	$O_\mu-Mn-O_{ac1}$	93.30
$O_1-Mn_2-N_4$	99.6(3)	$O_\mu-Mn'-N_{out'}$	98.03
$O_1-Mn_2-N_6$	95.7(3)	$O_\mu-Mn'-N_{out'}$	98.03
$O_1-Mn_2-N_5$	177.1(2)	$O_\mu-Mn'-N_{in'}$	179.78
$O_1-Mn_2-O_3$	92.3(2)	$O_\mu-Mn'-O_{ac'}$	93.47
$O_1-Mn_2-O_5$	94.7(3)	$O_\mu-Mn'-O_{ac1'}$	93.47

B. Geometry of $[Mn^{III}Mn^{IV}O_2(Oac)(tacn)_2]^{2+}$

experimental geometry[d]		input geometry[e]	
	Distances, Å		
$Mn\cdots Mn'$	2.588(2)	$Mn\cdots Mn'$	2.59
$Mn-O_1$	1.817(5)	$Mn-O_\mu$	1.81
$Mn-O_{1'}$	1.808(4)	$Mn-O_{\mu1}$	1.81
$Mn-O_2$	2.079(5)	$Mn-O_{ac}$	2.08
$Mn-N_1$	2.135(6)	$Mn-N_{in}$	2.13
$Mn-N_2$	2.105(5)	$Mn-N_{out}$	2.11
$Mn-N_3$	2.110(5)	$Mn-N_{out1}$	2.11
	Angles, deg		
$Mn-O_1-Mn'$	91.1(1)	$Mn-O_\mu-Mn'$	91.14
$O_1-Mn-O_{1'}$	87.2(2)	$O_\mu-Mn-O_{\mu1}$	87.14
O_1-Mn-N_2	94.4(2)	$O_\mu-Mn-N_{out}$	95.31
O_1-Mn-N_3	175.6(2)	$O_\mu-Mn-N_{out1}$	176.87
N_1-Mn-N_2	81.8(2)	$N_{in}-Mn-N_{out}$	81.97
N_1-Mn-N_3	82.1(2)	$N_{in}-Mn-N_{out1}$	81.97
N_2-Mn-N_3	82.1(2)	$N_{out}-Mn-N_{out1}$	82.17
$N_3-Mn-O_{1'}$	96.3(2)	$N_{out1}-Mn-O_{\mu1}$	95.31
O_2-Mn-O_1	93.5(2)	$O_{ac}-Mn-O_\mu$	93.49
O_2-Mn-N_1	167.0(2)	$O_{ac}-Mn-N_{in}$	167.07
O_2-Mn-N_2	87.7(2)	$O_{ac}-Mn-N_{out}$	88.30
O_2-Mn-N_3	89.0(2)	$O_{ac}-Mn-N_{out1}$	88.30

[a] Reference 24, with original atom labelings. [b] Data reflect C_s symmetry with the symmetry plane defined by Mn, Mn′, and O_μ. [c] Prime denotes those atoms close to Mn′ rather than Mn, and atoms reflected into one another under the C_s mirror operation are denoted as O_{ac}, O_{ac1} and similarly for N, $O_{ac'}$. [d] Reference 22 with original atom labels. [e] Data reflect C_s symmetry with the symmetry plane defined by atoms Mn, Mn′, and O_μ, and atoms reflected into one another under the C_s mirror operation are denoted as O_μ, $O_{\mu1}$ and similarly for N.

to obtain C−H = 1.11 Å and N−H = 1.02 Å. In all other complexes, these TACN ligands were substituted for those present originally, matching the original positions of the nitrogen triad, using the computer program from INSIGHT II (Biosym Inc.). This proved possible with only very small changes in internal TACN geometry and preserves the experimental Mn−N bond lengths and angles.

2.5. Evaluation of Spin-Coupling Parameters. The manganese dimers are spin-coupled systems. In density functional theory, spin coupling in dinuclear transition metal complexes can be evaluated from the energy difference between a high-spin state, where the spins of the monomeric subunits are aligned parallel, and a broken symmetry state, where these two spin vectors are oppositely aligned.[54,58,59] As in the formal description of maganese oxidation states Mn(IV) and Mn(III), we allow the corresponding spin vectors to have the values $S_i = {}^3/_2$ and 2, respectively. These formal monomeric spin vectors are mainly suitable (with the exceptions noted below), since for each dimeric system, we have found a low-lying high-spin state for all the $Mn^{IV}{}_2$, $Mn^{IV}Mn^{III}$, and $Mn^{III}{}_2$ complexes, where the total spin $S = S_{max} = S_1 + S_2$, giving $S = 3, {}^7/_2, 4$, respectively.

For the mixed-valence $Mn^{IV}Mn^{III}$ complexes **2** and **3**, we have also found in each a very low-lying $S = {}^5/_2$ state well below $S = {}^7/_2$. This state is the result of coupling $S_1 = 1$, with intermediate site spin, to $S_2 = {}^3/_2$ in a parallel fashion. Although unexpected from the viewpoint of formal site spin vectors of $S_1 = 2$, $S_2 = {}^3/_2$, the former site spin vectors and total spin are consistent with the net Mn site spins, and with the minority electron spin populations found in the broken symmetry state for complexes **2** and **3**. For these cases, the implications of finding the low-lying $S = {}^5/_2$ below $S = {}^7/_2$ will be examined.

By oppositely aligning the various spin vectors, and solving the SCF problem, we obtain broken symmetry states. Broken symmetry and high-spin calculations are used with spin projection methods to obtain the J parameter. For mixed-valence complexes, spin-dependent electron delocalization (called double exchange or resonance delocalization) is also possible.[54,58−60] Resonance delocalization is strongest in the high-spin state, where the main spin vectors on the halves of the molecule are parallel aligned. Therefore, we have calculated the double exchange parameter B from an orbital energy difference within the high spin state. (This procedure is applicable either to $S = {}^5/_2$ or ${}^7/_2$ in mixed-valence $Mn^{III}Mn^{IV}$ complexes. These differ in orbital occupancy by assigning the electron of the HOMO either to the relevant minority spin or majority spin orbital for $S = {}^5/_2$ and ${}^7/_2$, respectively.)

Typically, spin coupling in transition metal dimers is evaluated by determining the Heisenberg coupling constant J in the spin Hamiltonian

$$H = -2J\vec{S}_1\cdot\vec{S}_2 \qquad (1)$$

where $\vec{S}_1$, $\vec{S}_2$ are the spin vectors of the monomer subunits, formally attributed to the two metal ions. (We have adopted here the definition of the Heisenberg coupling parameter most common in the manganese dimer literature. We note that often in other work,[54,58] we have used another definition, particularly, $H = J'S_1\cdot S_2$, which just amounts to the redefinition $J' = -2J$.) The J coupling constant determines the entire ladder of spin states of the coupled system, with relative energies

$$E(S) = -JS(S+1) \qquad (2)$$

The mathematical and physical justification for the broken symmetry method and the spin projection procedure for extracting pure spin states has been discussed in detail in previous work.[54,58,59] The basic ideas and final equations, however, are quite simple, and are summarized below. Also, the physical meaning and use of the resonance delocalization (B term) has some subtle features as analyzed later. We represent the antiferromagnetic state of a spin-coupled system in density functional theory by a "broken symmetry" state. A spin unrestricted set of orbitals is occupied so that spin-up orbitals appear predominately on half of the molecule and spin-down orbitals on the other half. In practice, a spin-unrestricted high-spin calculation on the system is performed first, and then one of the site spin vectors is effectively rotated to an antiparallel alignment by interchanging the spin-up (α) and spin-down (β) densities on that site. Then the "broken symmetry" state is converged within a self-consistent-field (SCF) framework, as for the high-spin state. The broken symmetry state is a mixture of pure spin states. Since the weighting factors for these pure spin states are known, the energy difference can be expressed as a multiple of the J parameter. (The weights are Clebsch−Gordan (CG) coefficients for the expansion of the broken symmetry wave function in pure spin states and squares of CG coefficients for the expansion of the broken symmetry energy, E_B in pure spin energies, $E(S)$). Overall, we can formulate an equation

(58) Noodleman, L.; Case, D. A. *Adv. Inorg. Chem.* **1992**, *38*, 423−470.
(59) Noodleman, L.; Baerends, E. J. *J. Am. Chem. Soc.* **1984**, *106*, 2316−2327.
(60) Blondin, G.; Girerd, J. J. *Chem. Rev.* **1990**, *90*, 1359−1376.

Table 3

A. Comparison of Calculated J(cor) and J(uncor) with J(expt) (All cm^{-1}) for TACN Mn−Oxo Complexes

complex	calc J(cor)[a]	calc J(uncor)[a]	J(expt)[a]
$[Mn^{III}_2(\mu\text{-}O)(OAc)_2(TACN)_2]^{2+}$	−30	−30	10[b]
$[Mn^{III}Mn^{IV}(\mu\text{-}O)(OAc)_2(TACN)_2]^{3+}$, $S = {}^5/_2$	−200	66	−40[c]
$[Mn^{III}Mn^{IV}(\mu\text{-}O)(OAc)_2(TACN)_2]^{3+}$, $S = {}^7/_2$	−281	−218	−40[c]
$[Mn^{III}Mn^{IV}(\mu\text{-}O_2)(OAc)(TACN)_2]^{2+}$, $S = {}^5/_2$	−653	−390	−220[d]
$[Mn^{III}Mn^{IV}(\mu\text{-}O)_2(OAc)(TACN)_2]^{2+}$, $S = {}^7/_2$	−405	−355	−220[d]
$[Mn^{IV}_2(\mu\text{-}O)_2(\mu\text{-}O_2{}^{2-})(TACN)_2]^{2+}$	−232	−232	−120[e]
$[Mn^{IV}_2(\mu\text{-}O)_3(TACN)_2]^{2+}$	−689	−689	−390[f]

B. Estimated J_{eff} for Partial or Complete Delocalization

complex	J_0	B^2/E_{op}	J_{eff}^{pdeloc}	J_{eff}^{deloc}
	Ladder Based on $S = {}^5/_2$			
$[Mn^{III}Mn^{IV}(\mu\text{-}O)(OAc)_2(TACN)_2]^{3+}$ [g]	−200	40	−160	−23
$[Mn^{III}Mn^{IV}(\mu\text{-}O)_2(OAc)(TACN)_2]^{2+}$	−653	39	−614	−478
	Ladder Based on $S = {}^7/_2$			
$[Mn^{III}Mn^{IV}(\mu\text{-}O)(OAc)_2(TACN)_2]^{3+}$ [g]	−281	5	−276	−218
$[Mn^{III}Mn^{IV}(\mu\text{-}O)_2(OAc)(TACN)_2]^{2+}$	−405	3	−402	−355

[a] cm^{-1}. [b] $(ClO_4)_2$ counterion: see ref 56. [c] Tri-*N*-methyl−TACN and $(ClO_4)_3$ counterion: see ref 24. [d] $(B(C_6H_5)_4)_2$ counterion: see ref 22. [e] Estimated from the measured effective magnetic moment at two different temperatures: $1.2\mu_B$ at 81 K and $2.5\mu_B$ at 293 K: see ref 25. [f] Tri-*N*-methyl−TACN and (PF_6) counterion: see ref 38. [g] Using $1/\lambda = 7142$ cm^{-1} from $Mn^{III}Mn^{IV}(O_2CR)_2O(Me_3TACN)_2$: see ref 24.

$$E(S_{max} = S_1 + S_2) - E_B(M_S = S_1 - S_2) = -4JS_1S_2 \qquad (3)$$

for the energy difference between high spin and broken symmetry states. Here S_1 and S_2 are the spin quantum numbers for the monomeric subunits. J can then be extracted from the calculated energy difference on the left hand side of the equation.

This suffices when both transition metal sites have the same valence. The mixed valence dimer problem is more complex. The critical question here is whether the system has delocalized or localized mixed-valence, corresponding to Robin−Day class III or II respectively.[60,61] For a completely delocalized mixed-valence dimer, a more general spin Hamiltonian is

$$H = -2J_0S_1{\cdot}S_2 \pm B(S + {}^1/_2) \qquad (4)$$

with corresponding pure spin state energies

$$E(S)_{g,u} = -J_0S(S+1) \pm B(S + {}^1/_2) \qquad (5)$$

where S is the total spin quantum number of the dimer, and B is the resonance delocalization parameter. The first term is the Heisenberg coupling term, and the second is the resonance term. The ± represents the resonance g,u energy splitting (for minus, plus roots respectively) of a specific delocalized orbital. In density functional theory, the resonance term is absent in the broken symmetry state, but it is present in the high spin state where $S = S_{max}$. Here the resonance term is a maximum, and so this is the optimal way to calculate B in density functional theory; in fact, it is the only simple way to calculate this. The B parameter is then calculated from the resonance energy by

$$E(S_{max})_u - E(S_{max})_g = 2B(S_{max} + {}^1/_2) \qquad (6)$$

The corresponding J parameter is calculated by averaging out the B term in eq 5, taking

$$E(S_{max})_{av} = (E(S_{max})_g + E(S_{max})_u)/2 \qquad (7)$$

and then substituting into eq 3 (using $E(S_{max}) = E(S_{max})_{av}$) to obtain J_0. From eq 5, it is evident that the resonance g,u splitting increases linearly with total spin S. If the total spin S is small, then the resonance stabilization energy $-B(S + {}^1/_2)$ is also small, and the resonance effects can be effectively quenched by environmental effects including solvation, counterions, and vibronic coupling which produce an asymmetry between the metal sites.[60]

When the trapping energy ΔE_{trap} due to vibronic coupling, solvent reorganization, and other environmental effects strongly exceeds the resonance energies for all low-lying spin states, $\Delta E_{trap} \gg B(S + {}^1/_2)$, then the observed J coupling parameter (J_{eff}) will differ from J_0 by

$$J_{eff} = J_0 + (B^2/\Delta E_{trap}) \qquad (8)$$

giving a ferromagnetic (positive) shift due to the partial delocalization.[60,62] Energies evaluated from eq 8 will be specified by J_{eff}(pdeloc). For this strength of trapping, appropriate to a strongly trapped Robin−Day class II system, the trapping energy is the same as the energy of the intervalence charge transfer (IVCT) optical band $E_{op} = E_{trap}$,[60] which is observable at least in some systems. E_{op} is largely independent of the total spin state.

When the resonance energies $B(S + {}^1/_2)$ are comparable to ΔE_{trap}, the perturbative correction above is inadequate, and a more complex procedure is needed to determine the energies of the spin ladder.[60] The state energies in the completely delocalized limit (a Robin−Day class III system with a large resonance and no trapping energy) are given by eq 5. Taking the lower energy root for the B term in each spin state, and calculating the two lowest spin states (corresponding to $S_t = {}^1/_2, {}^3/_2$) J_{eff}(deloc) can be evaluated. In this case, the energy of the intervalence optical band becomes spin dependent $E_{op}(S_t) = 2B(S_t + {}^1/_2)$, and the band shape and spin-dependence of the transition moment are different from that in Robin−Day class II systems.

In the work that follows, J_0 and B will be calculated for the two mixed-valence complexes. The calculated value of J_0 will be referred to as the "corrected" J (J_{cor}). This equals J_{eff} in the localized valence limit (Robin−Day class I). Estimates of J_{eff} based on calculated B, J_0 values and estimated E_{op} will be computed for class II and III cases.

3. Results and Discussion

We will begin by relating the experimental structures to the calculated vs observed magnetic coupling parameters. The relationship of the magnetic coupling to the calculated manganese spin populations will also by developed. The calculated charges on the metal and ligand sites give insights into two important issues: (1) What is the extent of metal−ligand covalency, and how does charge transfer from each ligand to metal vary with the coordination geometry? Both the metal−ligand covalency and the charge transfer turn out to be very large compared with the results expected based on the formal metal oxidation state. (2) What roles do the different ligands play in creating the net ligand field at the metal? As we will show later, the ligand field strength at the two metal sites plays

(61) Robin, M. B.; Day, P. *Adv. Inorg. Chem. Radiochem.* **1967**, *10*, 247.

(62) Noodleman, L.; Case, D. A.; Mouesca, J.-M.; Lamotte, B. *J. Biol. Inorg. Chem.* **1996**, *1*, 177−182.

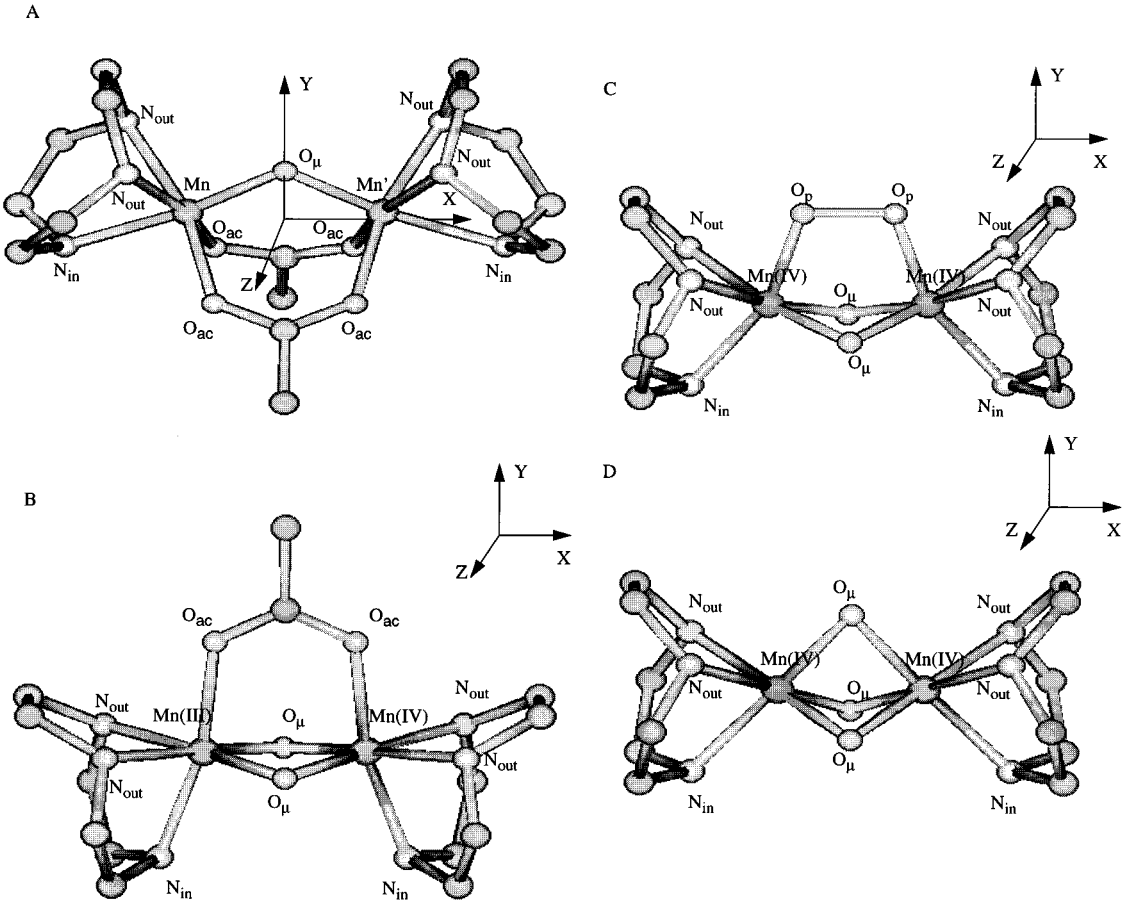

Figure 1. Structural diagrams of Mn−oxo TACN dimers for (a) complexes **1** and **2**, (b) complex **3**, (c) complex **4**, and (d) complex **5**.

an important part in setting both the manganese spin populations and establishing the strength of the magnetic coupling. There is, in fact, a competition between the strong spin polarization on each Mn site (the splitting between the majority spin vs minority spin levels) and the ligand field splitting on that site.

3.1. Summary of Geometric Issues. Table 1 shows the main bond lengths and angles for our calculations, all of which were performed in C_s point group symmetry corresponding to experimental geometries averaged for C_s. As the number of oxo ligands increase, there is a progressive shortening of the Mn−Mn distance, and the Mn−μ-O−Mn′ angle becomes more acute. The geometries of complexes **1** and **2** with one μ-O are rather similar, and very distinct from those of **3** and **4**, ((μ-O)$_2$) which are in turn distinct from that of **5** ((μ-O)$_3$). The three classes of Mn−Mn bond lengths are 3.1−3.2, 2.5−2.6, and 2.3 Å, while for angles, they are 120−125, 90, and 78°.

Structural diagrams for the different types of complexes are shown in Figure 1, which also shows the orientation of the coordinate system used in the calculations and analysis. Table 2 shows the experimental vs C_s model geometries for complexes **2** and **3**. While for **3**, $Mn^{III}Mn^{IV}$(μ-O)$_2$(OAc)(TACN)$_2$, the model and experimental geometries are quite close, for **2**, $Mn^{III}Mn^{IV}$$\mu$-O(OAc)$_2$(TACN)$_2$, the experimental Mn−O(Ac) distances show considerable variations, differing by about 0.05 Å, so that there is no overall molecular symmetry.

3.2. Heisenberg Coupling Parameters. Table 3 compares experimental versus calculated Heisenberg coupling parameters *J*. For the calculated *J* parameters, we have distinguished between "corrected" *J* values, calculated by averaging out the resonance *B* term, and "uncorrected" *J*'s, where the lowest high-spin state energy $E(S_{max})_g$ is used directly in the high-spin minus broken symmetry energy difference equation (eq 3). The two types of parameters differ only for the mixed-valence state $Mn^{III}Mn^{IV}$. Figure 2 is a scatter plot of the experimental vs calculated *J*. A linear least-squares fit between the calculated *J*(cor) and *J*(expt) values gives a fit with a correlation coefficient $r^2 = 0.914$ (Figure 2A) when the spin $S = {}^7/_2$ is used for S_{max}. When the *J* value for complex **2** is evaluated on the basis of the energy difference equation with $E(S_{max})_{av} - E_B$ for the lower energy $S_{max} = {}^5/_2$ state (eq 3 then gives $-6J$), $J_{cor} = -200$ cm^{-1}, for complex **2**, in place of the higher energy $S = {}^7/_2$ ($-12J$), with $J_{cor} = -281$ cm^{-1} compared with the lower experimental value *J*(expt) = -40 cm^{-1} (Table 3 and Figure 2B.) For complex **3**, the corresponding terms are $J_{cor} = -653$, -405 cm^{-1} for $S_{max} = {}^5/_2$, ${}^7/_2$ compared with *J*(expt) = -220 cm^{-1}. The correlation coefficient of the scatter plot is a little poorer for $S_{max} = {}^5/_2$ with $r^2 = 0.865$ (Figure 2B), because the calculated *J*(cor) for complex **3** deviates more from experiment than for $S_{max} = {}^7/_2$.

Below, we discuss the physical implications of the $S_{max} = {}^5/_2$ vs ${}^7/_2$ results for both *J* and *B* values. We note that both the low energy of $S_{max} = {}^5/_2$ and the fact that the Mn site spin distribution in the $S = {}^5/_2$ is closer to that in the broken symmetry state (compared to the $S = {}^7/_2$) favor this energy difference (particularly for complex **2**), and consequently the coupling scheme $S_1 = {}^3/_2$, $S_2 = 1$ is favored over the formally expected coupling scheme $S_1 = {}^3/_2$, $S_2 = 2$.

There are three important aspects of the mixed-valence systems and their spin coupling that deserve closer attention. These are as follows: (1) the question of trapping vs delocalization with consequences for J_{eff}; (2) the question of the geometric differences in the coordination geometry of the two Mn sites; (3) the physical status of the $S = {}^5/_2$ vs ${}^7/_2$ spin ladders for complexes **2** and **3**. In Table 3B, we give estimates of J_{eff} based on the influence of the resonance *B* term, and the trapping energy ΔE_{trap} using either eq 8 for partial delocalization

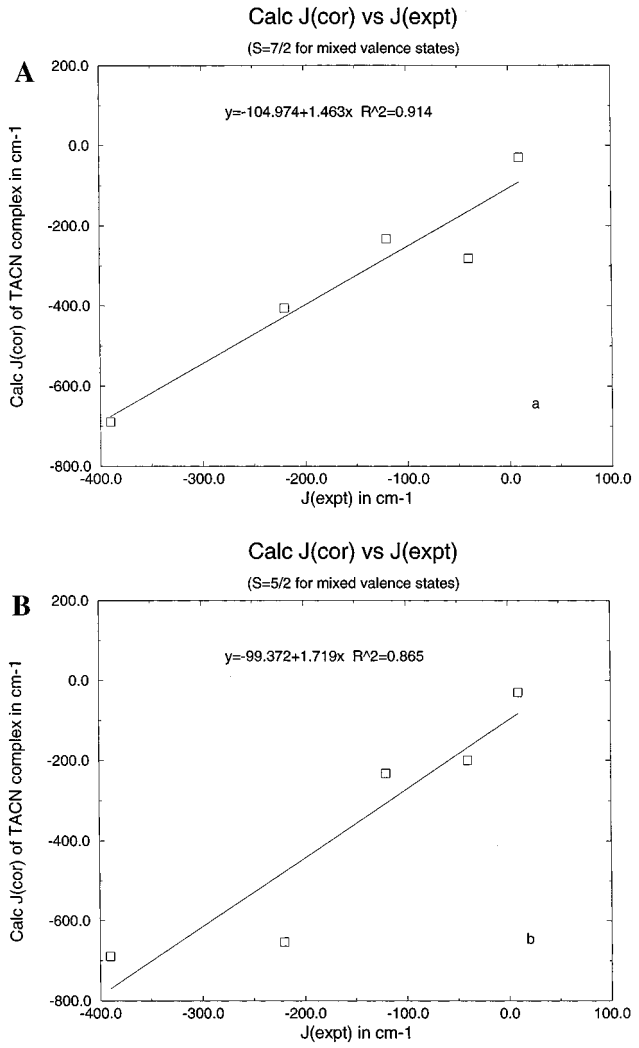

Figure 2. Scatter plot of calculated *J*(cor) parameters vs experimental. In the plots, high spin states $S = {}^7/_2$ (A) and $S = {}^5/_2$ (B) were used for the mixed valence states.

J_{eff}(pdeloc) or eq 5 for full delocalization J_{eff}(deloc). When we assume that complexes **2** and **3** are Robin−Day class II, the correction terms lead to a moderate reduction in the magnitude of J_{eff}, comparing J_0 with J_{eff}(pdeloc). By contrast, if total delocalization is assumed (Robin−Day class III), there is a much larger decrease in the magnitude of J_{eff}, which is particularly significant for complex **2** where the calculated J_{eff}(deloc) $= -23$ cm^{-1} compared with $J_0 = -200$ cm^{-1}. However, it appears most likely that complexes **2** and **3** and related systems are all Robin−Day class II and that the two Mn sites of complexes **2** and **3** are less geometrically equivalent than is apparent from the available X-ray structures.[1]

Since $\Delta E_{trap} = E_{op}$,[60] the energy of the intervalence charge transfer (IVCT) band for a Robin−Day class II system, reliable experimental results for these would be very valuable. In fact, the IVCT band energy is difficult to assess for complexes **2** and **3**. For complex **2**, an IVCT band has been assigned at an energy of 7142 cm^{-1}.[24] (This value was used to calculate J_{eff}(pdeloc) for both complexes **2** and **3** in Table 3B despite its tentative nature.) For complex **3**, no IVCT band has been assigned, and for related $Mn^{III}Mn^{IV}O_2$ complexes, Gamelin et al.[4] have not found an IVCT band, instead assigning the related band at 9800−12900 cm^{-1} as Mn(III) d → d. Their results cast doubt also on the IVCT assignment in the Mn(III,IV) systems $[L_2MnO_2MnL_2]^{3+}$, where L = 2,2′-bipyridine or 1,10-phenanthroline, where an IVCT band at 12 000 cm^{-1} was assigned earlier by Cooper and Calvin.[63,64] Overall, there are considerable uncertainties about the assignment of IVCT bands in these systems.

For the mixed-valence complexes **2** and **3**, the Mn−μ-O bond lengths and other Mn−L bond lengths (for example, the axial elongation of Mn(III)−L vs Mn(IV)−L bonds) reported from the X-ray structures (Tables 1 and 2) show only small differences between Mn sites, which is anomalous compared with other known $Mn^{III}Mn^{IV}$ mixed-valence systems.[1,65] It is likely that the nearly equal site geometries observed are the result of crystallographic averaging over larger Mn(III)−Mn(IV) geometry differences, since the Mn(III) and Mn(IV) sites are probably not ordered from one molecule to the next in the crystal. This is further supported by the observed disorder in the counterion environment of complex **2**.[24] It is then very difficult to know how different the two Mn site geometries are or what the effect would be on the calculated J values. This issue is also connected to the energy of trapping (ΔE_{trap}), although this energy involves both vibronic effects and solvent-counterion stabilization of the double-well potential.

The third issue is the interpretation of the $S_{max} = {}^5/_2$ vs $S_{max} = {}^7/_2$ based Heisenberg spin ladders for complexes **2** and **3**. Since the energy of the $S_{max} = {}^5/_2$ is lower in each case, and the resemblance to the broken symmetry state composition is closer for $S_{max} = {}^5/_2$, this provides our best estimate of the lowest lying Heisenberg spin ladder. Further, we have examined the symmetry of the HOMO for the broken symmetry (BS), $S_{max} = {}^7/_2$, and $S_{max} = {}^5/_2$ electronic configurations for both complexes. The HOMO is particularly important since it is the electron in this orbital that can potentially delocalize when the trapping barrier is low. The HOMO of the higher spin state in these mixed-valence systems should have the same symmetry (with respect to the C_s point group) as that in the BS state if they belong to the same spin ladder.

For complex **2**, the HOMO of $S_{max} = {}^7/_2$ has A″ symmetry, which differs from the A′ symmetry of the BS(ground state) HOMO. Instead, the HOMO of $S_{max} = {}^7/_2$ correlates with the first excited BS state orbital, 39A″. This means that BS(ex1) and $S_{max} = {}^7/_2$ should be used to construct the Heisenberg ladder of the excited state rather than the ground state. A straightforward SCF difference calculation and related analysis yields an excited state 48A′β → 39A″β with calculated energy ΔE_{SCF}(BS) = 0.34 eV, $\Delta E_{SCF}(S = {}^1/_2) = 0.43$ eV, and excited state J_{cor}(ex1) $= -53$ cm^{-1}. From these results, this excited Heisenberg ladder is too high lying to be thermally populated; however, it may interact with the ground-state spin ladder through a pseudo-Jahn−Teller interaction.

For complex **3**, the HOMO's of BS(ground state), $S_{max} = {}^5/_2$, $S_{max} = {}^7/_2$, all have A′ symmetry. Further, the BS HOMO has nearly equal contributions from both Mn sites, and therefore has nearly equal majority spin and minority spin contributions since the spin vectors of the sites are oppositely aligned. Two Heisenberg ladders based on $S_{max} = {}^5/_2$ and $S_{max} = {}^7/_2$ may coexist. Alternatively, configuration mixing of these two Heisenberg ladders may occur for all states where $S \leq {}^5/_2$ so that only one low-lying spin ladder would be found. The J coupling calculated for both $S_{max} = {}^5/_2$ and $S_{max} = {}^7/_2$ ladders are given for complexes **2** and **3**. The detailed Mn spin composition and energy level structures are analyzed later.

(63) Cooper, S. R.; Calvin, M. *J. Am. Chem. Soc.* **1977**, *99*, 6623−6630.
(64) Cooper, S. R.; Dismukes, G. C.; Klein, M. P.; Calvin, M. *J. Am. Chem. Soc.* **1978**, *100*, 7248−7252.
(65) Plaksin, P. M.; Stoufer, R. C.; Mathew, M.; Palenik, G. J. *J. Am. Chem. Soc.* **1972**, *94*, 2121−2122.

Table 4

A. Comparison of Calculated J Values (cm^{-1}) of TACN-Complexed and "Core Only" Mn−Oxo Dimers

	core		TACN-complex	
complex	J(cor)	J(uncor)	J(cor)	J(uncor)
$[Mn^{III}_2(\mu\text{-}O)(OAc)_2]^{2+}$	45	45	−30	−30
$[Mn^{III}Mn^{IV}(\mu\text{-}O)(OAc)_2]^{3+}$, $S = {}^5/_2$	−831	−630	−200	66
$[Mn^{III}Mn^{IV}(\mu\text{-}O)(OAc)_2]^{3+}$, $S = {}^7/_2$	130	247	−281	−218
$[Mn^{III}Mn^{IV}(\mu\text{-}O)_2(OAc)]^{2+}$, $S = {}^5/_2$	−1695	−1020	−653	−390
$[Mn^{III}Mn^{IV}(\mu\text{-}O)_2(OAc)]^{2+}$, $S = {}^7/_2$	−159	−59	−405	−355
$[Mn^{IV}_2(\mu\text{-}O)_2(\mu\text{-}O_2^{2-})]^{2+}$	−65	−65	−232	−232
$[Mn^{IV}_2(\mu\text{-}O)_3]^{2+}$	−614	−614	−689	−689

B. Comparison of B Values (cm^{-1}) of TACN-Complexed and "Core Only" Mn−Oxo Dimers

complex	core	TACN complex[a]
$[Mn^{III}Mn^{IV}(\mu\text{-}O)(OAc)_2]^{3+}$, $S = {}^5/_2$	401	532
$[Mn^{III}Mn^{IV}(\mu\text{-}O)(OAc)_2]^{3+}$, $S = {}^7/_2$	352	189
$[Mn^{III}Mn^{IV}(\mu\text{-}O)_2(OAc)]^{2+}$, $S = {}^5/_2$	1350	526
$[Mn^{III}Mn^{IV}(\mu\text{-}O)_2(OAc)]^{2+}$, $S = {}^7/_2$	300	149

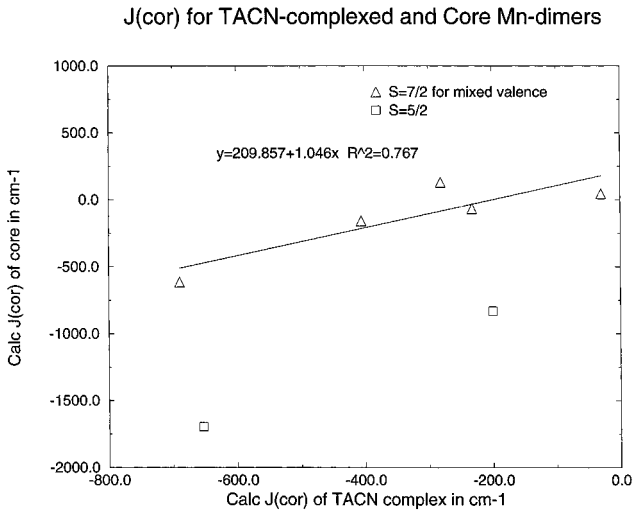

Figure 3. Calculated J parameters for the TACN complexes vs core-only dimers. The straight line was fit including data points of $S = {}^7/_2$ spin states rather than $S = {}^5/_2$ (also shown, since the former have lower energies in the core systems).

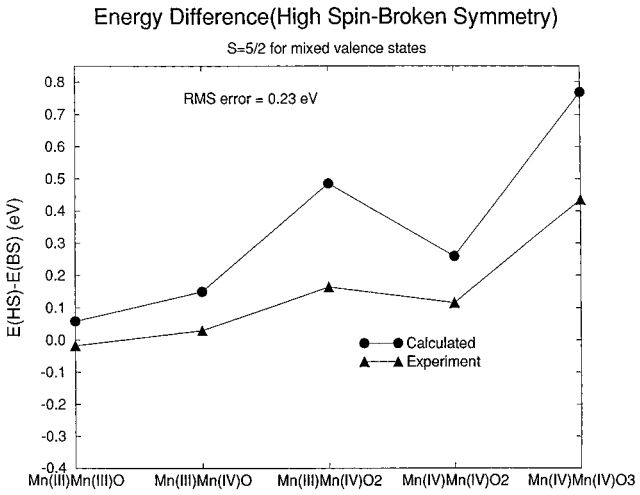

Figure 4. Calculated energy differences, E(HS) − E(BS), vs "experimental" data with the latter being evaluated from eq 3 in the text with assumed monomer spin states.

For the collection of five complexes studied (and whether $S = {}^5/_2$ or ${}^7_2$ is used for the upper spin state of the mixed-valence systems), there is a systematic trend for the calculated J values to show stronger antiferromagnetic coupling than seen experimentally. This behavior is consistent with what we have seen previously in dinuclear and polynuclear iron−sulfur clusters, where calculated J parameters are typically larger than those found experimentally.[54,58,59] However, in the present Mn−oxo dimers, we possess a larger series of purely dinuclear complexes where this comparison can be made, without the complicating influences present in polynuclear systems with four metal ions as in the Fe_4S_4 clusters[54,58,59] and Mn−oxo (Mn_4O_3) cubane systems.[66]

Table 4A and Figure 3 compare the J values calculated for the complete complexes containing the TACN ligands with those for the corresponding "core-only" complexes where these terminal ligands have been omitted. Table 4B gives the calculated resonance delocalization B parameters calculated from the high-spin states of the complete and core only complexes. There is a reasonable linear correlation between the J values of the core and complete complexes, with a substantial ferromagnetic shift for the core-only compared to the complete systems. The main point here is the general trend and the strong ferromagnetic shift seen in the core systems. We can attribute this to the much weaker ligand fields of the core complexes, since the TACN ligands cause considerable splitting of the Mn d orbitals.

We can put the energetic results in some perspective by looking at the actual energy evaluation procedure, which uses the energy difference $E(S_{max}) - E_B$ corresponding to $-16J$ for the Mn^{III}_2 system, $-6J$ for $Mn^{III}Mn^{IV}$ when $S_{max} = {}^5/_2$ and $-9J$ for Mn^{IV}_2 systems. When the experimental J values are also translated into an "experimental" $E(S_{max}) - E_B$, the experimental range is from −0.02 to 0.44 eV, while the calculated range is from 0.06 to 0.72 eV. The RMS error is 0.23 eV. This size of error is comparable to that found for ionization and excitation energies in transition metal complexes by density functional methods.[67] Further, the RMS error we have calculated for the E(HS) − E(BS) energy difference is comparable to that found for bridged $Fe^{III}_2(\mu\text{-}O)$ complexes using ab initio calculations and the broken symmetry method.[68,69] We are then trying to obtain energy differences to an accuracy of about 0.1 eV, while the total binding energies of the complexes are of the order of 300−350 eV with respect to spin restricted atoms. In Figure 4, this energy difference is plotted for the five different complexes.

(66) Schmitt, E. A.; Noodleman, L.; Baerends, E. J.; Hendrickson, D. N. *J. Am. Chem. Soc.* **1992**, *114*, 6109−6119.

(67) Ziegler, T. *Can. J. Chem.* **1995**, *73*, 743−761.

(68) Hart, J. R.; Rappe, A. K.; Gorun, S. M.; Upton, T. H. *Inorg. Chem.* **1992**, *31*, 5254−5259.

(69) Alder, J.; Ensling, J.; Gutlich, P.; Bominaar, E. L.; Guillin, J.; Trautwein, A. X. *Hyperfine Interact.* **1988**, *49*, 869.

For complex **1**, the calculated J value, -30 cm^{-1} is weakly antiferrogmanetic, while J(expt) $= 10$ cm^{-1} is weakly ferromagnetic. Hotzelmann and co-workers[70] have used qualitative orbital interaction arguments in a series of dinuclear complexes and have argued for the importance of a cross-interaction which will contribute a substantial ferromagnetic term to the spin-coupling interaction of complex **1**. The mechanism which they invoke is broadly consistent with the energy level pattern we have found (Figure 10 and 14), and such terms will contribute to the high-spin minus broken symmetry energy difference. It appears that the incorrect sign of J for complex **1** arises because of the sensitive balance of antiferromagnetic (AF) and ferromagnetic (F) terms.

For complex **5**, Mn(IV)$_2$(μ-O)$_3$, the three (μ-O) bridges form a set of effective exchange pathways. Strong J coupling is predicted and found, although J(calc) $= -689$ cm^{-1} substantially exceeds J(expt) $= -390$ cm^{-1}. Since the calculation employed a spin ladder with $S_{max} = 3$, we have also performed separate calculations on various excited $S_{max} = 2$ states using the Slater[71,72] transition state scheme for the $S_{max} = 3 \rightarrow S_{max} = 2$ excitation. This tests whether there is an alternative lower spin ladder, effectively with one strong valence bond (molecular orbital like) and two weaker valence bonds, $S_1 = S_2 = 1$, $S_{max} = 2$, in place of three valence bonds (appropriate for $S_{max} = 3$ with $S_1 = S_2 = {}^3/_2$). We found that all $S_{max} = 2$ states are higher than $S_{max} = 3$, with the lowest 0.08 eV above $S_{max} = 3$, so the $S_{max} = 3$ spin ladder is more appropriate theoretically. The $S_{max} = 2$ ladder yields an even larger J(calc) $= -1711$ cm^{-1}, so this hypothesis does not provide a better correlation with experiment. Instead, it appears that the VBP exchange-correlation potential that we are using systematically overestimates the antiferromagnetic coupling strength, but in a fairly consistent manner.

The main physical interactions involved in spin coupling and their net effects include the following:[60,66] (a) direct exchange (F), (b) superexchange (AF), (c) "crossed superexchange" interaction (F),[70] (d) ligand spin polarization (either AF or F), and also (e) resonance delocalization (or "double exchange") (F) in mixed-valence systems. The competition between mechanisms b, d, and c are quite important for the sign and strength of AF versus F coupling. The important influences are shown in the following analysis. The spin-coupling pathways conserve the spin index (α or β) for all orbitals in both the HS and BS states. (We will also consider for simplicity that "conceptually prior" to the occurrence of the spin-coupling exchange interactions, the acceptor Mn(3d) orbitals are mainly empty, although both ligand field effects and spin-coupling mechanisms lead "finally" to partial occupancy of all Mn(3d) components.) In the BS state, metal-to-metal charge transfer from filled majority spin metal orbitals on one site to (mainly empty) minority spin metal orbitals on the opposite site provides energetic stabilization. These are superexchange interactions since these orbitals contain ligand contributions. Furthermore, other mainly ligand orbitals contribute bridging ligand-to-metal charge transfer interactions, donating into the empty minority spin metal orbitals (ligand spin polarization). In the HS state, the principal metal-to-metal charge transfer proceeds from majority spin (filled) to majority spin (mainly empty) orbitals, and the largest contribution is from $t_{2g} \rightarrow e_g$ (filled $\rightarrow$ mainly empty), as in the proposed cross-exchange mechanism for ferromagnetic pathways. Ligand-to-metal (e_g) charge-transfer mechanisms also contribute here. These stabilize the HS state. Clearly, the accessibility in energy of the empty minority spin metal orbitals compared to empty (e_g) majority spin orbitals is a direct function of the strength of the ligand field splitting $e_g - t_{2g}$ compared to the spin polarization splitting (α vs β on a Mn site). The total ligand field from both bridging and terminal ligands determines the ligand field splitting. Since, in the fully interacting spin-coupled system, all Mn(3d) orbitals will be partially occupied, population analyses are helpful in assessing ligand field effects and metal-to-metal as well as ligand−metal charge transfer (covalency).

3.3. Manganese 3d and Spin Populations. While total atomic charges can be obtained either using ESP fitting charges or from Mulliken population analysis, separate α and β populations, net spin $\alpha - \beta$ populations, and a breakdown into contributions from Mn 3d, 4s, and 4p orbitals can be derived only from the Mulliken analysis. These are presented in Table 5. Figure 5 shows the corresponding total α spin, β spin, and net spin populations graphically both with and without TACN. Comparing the complete and core-only complexes, some related trends are evident: (1) the net spin populations for each complete complex are always less than those for the corresponding core-only system; (2) the net Mn spin populations decrease with increasing oxidation state and number of oxo-ligands; (3) the largest contributor to this effect is an overall increase in the minority spin population; (4) the minority spin populations for the broken symmetry system exceed those for the corresponding high-spin configurations, and the net spin populations are smaller for the broken symmetry states. Since the overall ligand field strength of the complete complexes is much larger than for the core-only systems, there is more charge and spin transfer for the former, and an overall increase in minority spin populations on the manganese sites. Increasing AF coupling is also largely but not completely correlated with lower net spin populations and larger minority spin populations in the BS state. The exception to this rule is complex **4**, the peroxo $Mn^{IV}_2(\mu\text{-}O)_2(\mu\text{-}O_2)$ system, which according to both our calculations and experiment has a considerably weaker AF coupling than the mixed-valence complex **3** $Mn^{III}Mn^{IV}(\mu\text{-}O)_2(OAc)_1$. The data analysis in the next section shows that the peroxo ligand $(O_2)^{2-}$ is a much stronger charge donor than acetate and peroxo is a stronger spin donor in the high spin state; these effects probably contribute to the weaker AF coupling of complex **4** compared with **3**.

In these systems, Mn(III) and Mn(IV) are the "conventional" (or "formal") oxidation states, those that are consistent with the total electron count, and with the formal charges on the ligands (O^{2-} for oxo, $O_2{}^{2-}$ for peroxo, etc.) (See, for example, the discussion of the difference between "formal" and more "realistic" charge distributions, and the relationship to Pauling's electroneutrality principle in Gerloch and Constable.)[73] Ultimately, the ideal HS Mn(IV,III,II) ion occupation schemes can be traced back to a purely ionic "crystal field" picture, which is limited by neglect of charge transfer, superexchange, and related effects. Ideal high-spin (HS) Mn ions have the occupation scheme Mn(IV) $d^3\alpha$ ($S = {}^3/_2$), Mn(III) $d^4\alpha$ ($S = 2$), and Mn(II) $d^5\alpha$ ($S = {}^5/_2$) (used in ligand field descriptions of electronic structure and spectroscopy), but there are a number of other Mn ion oxidation and spin states that can be significant. These are summarized in Scheme 1. With calculated majority spin Mn 3d populations about 4−5, and minority spin popula-

(70) Hotzelmann, R.; Wieghardt, K.; Flörke, U.; Haupt, H.-J.; Weatherburn, D. C.; Bonvoisin, J.; Blondin, G.; Girerd, J.-J. *J. Am. Chem. Soc.* **1992**, *114*, 1681−1696.
(71) Slater, J. C. *Adv. Quantum Chem.* **1972**, *6*, 1.
(72) Slater, J. C. *The Self-Consistent Field for Molecules and Solids: Quantum Theory of Molecules and Solids*; McGraw-Hill: New York, 1974.
(73) Gerloch, M.; Constable, E. C. *Transition Metal Chemistry*; VCH: Weinheim, Germany, 1994.

Table 5. Spin Populations on Manganese Ions of the TACN Complexes

		α		β		α−β	
complex	atom	S, P, D	tot.	S, P, D	tot.	D	tot.
			A. TACN Complexes				
			BS				
1	MnA	0.113, 0.298, 4.463	4.874	0.052, 0.193, 0.866	1.111	3.597	3.763
	MnB	0.052, 0.192, 0.862	1.105	0.114, 0.300, 4.466	4.881	−3.604	−3.776
2	MnA	0.053, 0.219, 1.227	1.499	0.102, 0.308, 4.110	4.520	−2.883	−3.021
	MnB	0.092, 0.281, 3.740	4.113	0.053, 0.215, 1.714	1.982	2.026	2.131
3	MnA	0.086, 0.279, 4.229	4.593	0.039, 0.186, 1.133	1.358	3.096	3.235
	MnB	0.043, 0.189, 1.633	1.865	0.085, 0.268, 3.810	4.162	−2.177	−2.297
4	MnA	0.073, 0.252, 3.905	4.230	0.035, 0.175, 1.457	1.667	2.448	2.563
	MnB	0.036, 0.176, 1.453	1.665	0.074, 0.254, 3.908	4.235	−2.431	−2.571
5	MnA	0.078, 0.242, 3.886	4.206	0.036, 0.174, 1.490	1.700	2.396	2.506
	MnB	0.038, 0.176, 1.489	1.703	0.077, 0.240, 3.882	4.199	−2.392	−2.496
			HS[a]				
1	MnA	0.109, 0.297, 4.506	4.912	0.058, 0.196, 0.811	1.065	3.695	3.847
	MnB	0.109, 0.297, 4.505	4.911	0.058, 0.197, 0.812	1.067	3.693	3.844
2	MnA	0.103, 0.309, 4.279	4.692	0.057, 0.216, 1.023	1.297	3.256	3.395
		(0.095, 0.290, 3.917	4.302	0.058, 0.217, 1.477	1.752	2.440	2.550)
	MnB	0.102, 0.314, 4.293	4.709	0.056, 0.219, 1.004	1.279	3.289	3.430
		(0.094, 0.295, 3.928	4.317	0.056, 0.220, 1.464	1.740	2.464	2.577)
3	MnA	0.083, 0.278, 4.212	4.573	0.042, 0.196, 1.130	1.368	3.082	3.205
		(0.073, 0.261, 3.863	4.196	0.0433, 0.197, 1.555	1.795	2.308	2.402)
	MnB	0.091, 0.279, 4.283	4.653	0.046, 0.188, 1.046	1.280	3.237	3.373
		(0.077, 0.261, 3.864	4.202	0.049, 0.196, 1.553	1.798	2.310	2.404)
4	MnA	0.070, 0.250, 3.957	4.277	0.040, 0.182, 1.388	1.610	2.569	2.667
	MnB	0.070, 0.249, 3.955	4.273	0.039, 0.180, 1.391	1.610	2.564	2.663
5	MnA	0.078, 0.257, 4.027	4.362	0.039, 0.173, 1.300	1.512	2.727	2.850
	MnB	0.076, 0.255, 4.022	4.353	0.038, 0.172, 1.302	1.512	2.720	2.841
			B. "Core Only" Complexes				
			BS				
1	MnA	0.104, 0.142, 4.523	4.770	0.057, 0.090, 0.762	0.909	3.761	3.861
	MnB	0.058, 0.090, 0.762	0.910	0.104, 0.143, 4.522	4.769	−3.760	−3.859
2	MnA	0.080, 0.124, 4.516	4.720	0.036, 0.082, 0.704	0.821	3.812	3.899
	MnB	0.038, 0.084, 1.166	1.289	0.077, 0.110, 4.101	4.288	−2.935	−2.999
3	MnA	0.082, 0.119, 4.382	4.582	0.048, 0.077, 0.0882	1.007	3.500	3.575
	MnB	0.044, 0.076, 1.330	1.451	0.075, 0.101, 3.986	4.162	−2.656	−2.711
4	MnA	0.052, 0.069, 3.969	4.090	0.030, 0.051, 1.270	1.351	2.699	2.739
	MnB	0.030, 0.051, 1.261	1.342	0.053, 0.070, 3.975	4.090	−2.714	−2.748
5	MnA	0.038, 0.064, 3.950	4.052	0.027, 0.057, 1.292	1.376	2.658	2.676
	MnB	0.026, 0.057, 1.291	1.374	0.037, 0.065, 3.948	4.050	−2.657	−2.676
			HS				
1	MnA	0.107, 0.145, 4.578	4.831	0.058, 0.088, 0.685	0.832	3.893	3.999
	MnB	0.107, 0.146, 4.579	4.833	0.058, 0.089, 0.683	0.831	3.896	4.002
2	MnA	0.082, 0.122, 4.460	4.663	0.039, 0.082, 0.733	0.854	3.727	3.809
	MnB	0.084, 0.123, 4.466	4.674	0.040, 0.084, 0.728	0.852	3.738	3.822
3	MnA	0.094, 0.119, 4.320	4.533	0.045, 0.081, 0.921	1.047	3.399	3.486
	MnB	0.093, 0.119, 4.323	4.535	0.045, 0.080, 0.917	1.042	3.406	3.493
4	MnA	0.064, 0.072, 4.058	4.193	0.027, 0.051, 1.155	1.233	2.903	2.960
	MnB	0.063, 0.072, 4.058	4.193	0.027, 0.051, 1.155	1.233	2.903	2.960
5	MnA	0.058, 0.068, 4.056	4.182	0.018, 0.060, 1.133	1.211	2.923	2.971
	MnB	0.058, 0.072, 4.048	4.177	0.017, 0.059, 1.141	1.218	2.907	2.959

[a] The highest spin state except for values in parentheses which are the $^5/_2$ spin states.

tions of about 1−2, shown in Figure 5 and Table 5, we find that the most important Mn valence states contributing to the electronic structures of complexes **1**−**5** are as follows: $S_i = {}^3/_2$, intermediate-spin Mn(II), $d^4\ \alpha d^1\ \beta$; $S_i = 2$, high-spin Mn(I), $d^5\ \alpha d^1\ \beta$; and $S = 1$, intermediate-spin Mn(I) $d^4\ \alpha d^2\ \beta$. The total d electron count for each of these is higher than those for "conventional" Mn(III) and Mn(IV) states, and the total Mn charges are lower (Table 6). This is quite compatible with strong ligand → metal charge transfer particularly from oxo, peroxo, and TACN to the metal ions. Overall, our electronic structure calculations predict polar covalent bonding rather than purely ionic bonding using either Mulliken or electrostatic potential (ESP) based charge analysis. A weaker Mn ligand field is expected to favor a site spin of $S_i = 2$ over $S_i = 1$, and conversely a stronger ligand field would favor $S_i = 1$. The calculations indicate that we are near the site spin crossover region $S_i = 2 \rightarrow S_i = 1$, and that this crossover occurs upon Mn^{III} to $Mn^{III}Mn^{IV}$ oxidation, from complex **1** to complex **2**. In addition, this picture rationalizes the fairly close proximity of $S_{max} = {}^5/_2$ and $^7/_2$ states in the mixed-valence systems. Here

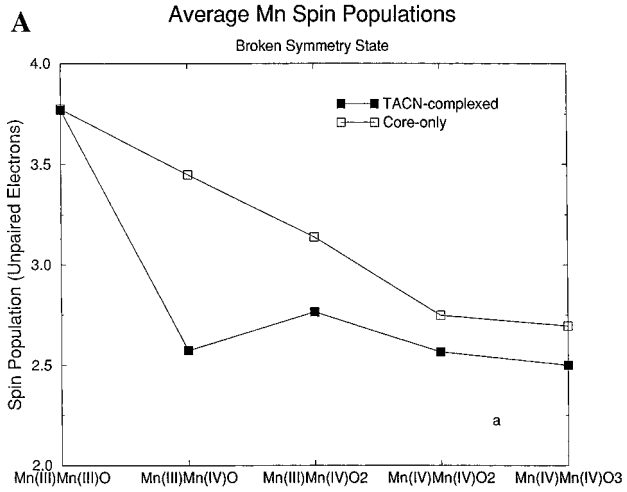

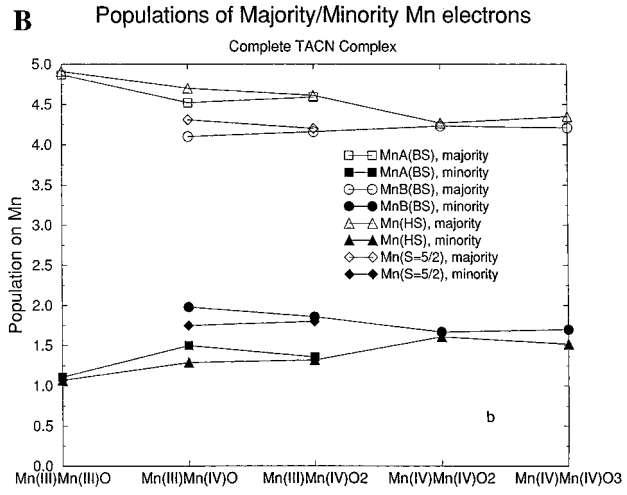

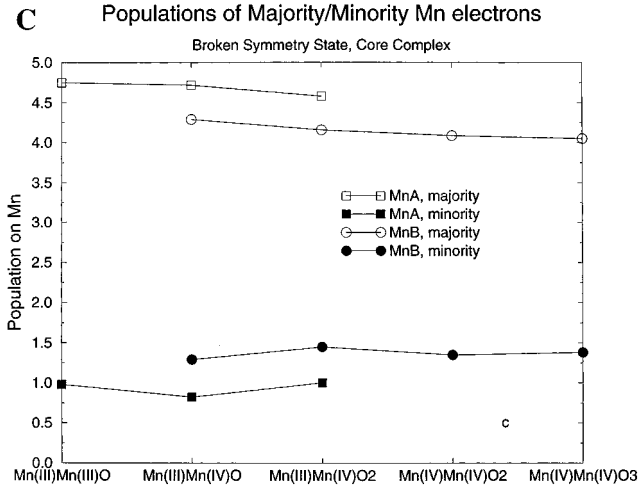

Figure 5. (a) Average spin populations of the manganese ions plotted for all five complexes, with and without TACN ligands. (b) Majority/minority spin populations of manganese electrons for TACN complexes. (c) Populations as in part b but for core-only complexes.

parallel alignment of $d^4\ \alpha d^2\ \beta$ with $d^4\ \alpha d^1\ \beta$ corresponds to parallel alignment of $S_1 = 1$ with $S_2 = {}^3/_2$ to give $S = {}^5/_2$ and delocalization of a minority spin electron, while parallel alignment of $d^5\ \alpha d^1\ \beta$ with $d^4\ \alpha d^1\ \beta$ corresponds to parallel alignment of $S_1 = 2$ with $S_2 = {}^3/_2$ to give $S = {}^7/_2$ and delocalization of a majority spin electron. (Table 5, HS for $S = {}^5/_2, {}^7/_2$ gives Mn(d) α and β spin populations completely consistent with this picture, noting that with delocalization, the Mn(A),Mn(B) site populations are averaged.) In the "conventional" scheme for Mn(III), Mn(IV) parallel alignment, $S = {}^7/_2$, there is delocalization of a majority spin electron as well, but the d electron count is different. The "core-only" complexes have much weaker ligand fields than the corresponding TACN complexes, and in both of the mixed-valence "core-only" complexes, the $S_{max} = {}^7/_2$ state is calculated to be well below $S_{max} = {}^5/_2$.

Scheme 1. Oxidation States and Spin States of Manganese Ions

S=2	1	3/2	5/2	
Mn(III) $d^4\alpha$	Mn(V) $d^2\alpha$	Mn(IV) $d^3\alpha$		Spin state type= HS[a]
Mn(I) $d^5\alpha d^1\beta$		Mn(0) $d^5\alpha d^2\beta$	Mn(II) $d^5\alpha$	HS[a]
	Mn(I) $d^4\alpha d^2\beta$	Mn(II) $d^4\alpha d^1\beta$		IS[b]

[a] HS = High Spin
[b] IS = Intermediate Spin

The total Mn(4s) + Mn(4p) population amounts to only about 10% of the total Mn(3d) population in the TACN complexes. However, the Mn(4p) population in the TACN complexes is considerably larger, by $0.2-0.3e^-$, than that in the core-only systems and accounts for roughly half of the increased electron density on manganese in the complete complexes. The weakened ligand fields of the core-only complexes therefore lead to a loss of electron density from these polarization functions which hydridize with the Mn(3d). When a comparison is made among the complete complexes, however, the Mn(4s) + Mn(4p) population slowly decreases with increasing Mn oxidation state and the number of oxo- or peroxo-ligands. Since the Mn(4p) population can affect the intensities of optical transitions or X-ray near edge spectroscopy (XANES) arising from core Mn(1s) → Mn(4p) dipole-allowed transitions these population differences should have observable consequences.

3.4. Charges on Important Groups and Charge Transfer. Figure 6 shows the calculated ESP charges for the Mn atoms in the complete and core-only complexes. In Table 6, the total Mn 3d,4s,4p Mulliken populations and Mulliken charges are given and compared with the ESP charges. These results are quite remarkable compared with the formal charges of +3,+4 for the manganese sites. The ESP charges on Mn for the TACN complexes are both much less than those expected from the formal oxidation states and mainly show a slow decrease with increasing formal oxidation state and with increasing numbers of μ-O ligands. This decrease is opposite to the trend expected from the formal oxidation states. In fact, only in the core systems does Mn charge increase with increasing oxidation state, and even this behavior is nonmonotonic. This trend for the TACN complexes reflects strong metal−ligand covalency and large electron relaxation effects. For example, complex **2** is obtained from complex **1** by removing one electron, yet the actual charges at the manganese sites increase only slightly. Most of the increase in positive charge appears instead on the TACN and carboxylate ligands.

In Figure 7, we show the charge transferred from each type of ligand to the metal, reported as the charge transferred per donor atom to a single metal site. The TACN charge transfer is then divided by 3 for the three nitrogen donors, the acetate group transfer by 2, each μ-O by 2, and the total peroxo transfer

Table 6. Populations and Charges on Manganese Ions

complex	atom	population			charge[a]	
		S	P	D	Mulliken	ESP
			A. TACN Complexes			
			BS			
1	MnA	0.165	0.491	5.329	1.014	1.213
	MnB	0.166	0.492	5.328	1.014	1.214
2	MnA	0.155	0.527	5.337	0.981	1.340
	MnB	0.145	0.496	5.454	0.905	1.240
3	MnA	0.125	0.465	5.362	1.048	1.217
	MnB	0.128	0.457	5.443	0.973	1.165
4	MnA	0.110	0.430	5.360	1.100	1.059
	MnB	0.108	0.427	5.363	1.103	1.047
5	MnA	0.114	0.416	5.376	1.091	1.051
	MnB	0.115	0.417	5.370	1.100	1.057
			HS[b]			
1	MnA	0.167	0.493	5.317	1.024	1.218
	MnB	0.167	0.494	5.317	1.022	1.218
2	MnA	0.16	0.525	5.302	1.012	1.343
		(0.153	0.507	5.394	0.946	1.280)
	MnB	0.158	0.533	5.297	1.012	1.329
		(0.150	0.515	5.492	0.943	1.269)
3	MnA	0.125	0.474	5.342	1.059	1.199
		(0.116	0.458	5.418	1.008	1.215)
3	MnB	0.137	0.467	5.329	1.066	1.215
		(0.124	0.456	5.417	1.000	1.216)
4	MnA	0.110	0.432	5.345	1.114	1.067
	MnB	0.109	0.429	5.346	1.117	1.056
5	MnA	0.117	0.430	5.327	1.122	1.057
	MnB	0.114	0.427	5.324	1.135	1.062
			B. "Core Only" Systems			
			BS			
1	MnA	0.161	0.232	5.285	1.322	1.536
	MnB	0.162	0.233	5.284	1.321	1.537
2	MnA	0.116	0.206	5.22	1.458	1.638
	MnB	0.115	0.194	5.267	1.423	1.667
3	MnA	0.13	0.196	5.264	1.411	1.494
	MnB	0.119	0.177	5.316	1.387	1.489
4	MnA	0.082	0.12	5.239	1.558	1.587
	MnB	0.083	0.121	5.236	1.560	1.587
5	MnA	0.065	0.121	5.242	1.571	1.598
	MnB	0.063	0.122	5.239	1.576	1.597
			HS			
1	MnA	0.165	0.233	5.263	1.337	1.549
	MnB	0.165	0.235	5.262	1.337	1.550
2	MnA	0.121	0.204	5.193	1.483	1.662
	MnB	0.124	0.207	5.194	1.474	1.660
3	MnA	0.139	0.2	5.241	1.420	1.499
	MnB	0.138	0.199	5.24	1.423	1.502
4	MnA	0.091	0.123	5.213	1.573	1.594
	MnB	0.09	0.123	5.213	1.574	1.594
5	MnA	0.076	0.128	5.189	1.607	1.621
	MnB	0.075	0.131	5.189	1.605	1.618

[a] In unit of $|e|$. [b] The highest spin state except for values in parentheses, which are for $^5/_2$ spin states.

by 2. The transfer charge is calculated using the formal ligand charge as the reference value. Figure 7B also shows the net charge transfer to each Mn atom using as reference values the average formal Mn oxidation state for that complex, either +3, +3.5, or +4. In this context, the charge transfer is very large and rises rapidly with increasing oxidation state and number of oxo ligands.

We have plotted the charge transfer from the ligands on a per donor atom basis because synthetic complexes and/or proteins often differ by replacement of one donor atom by another type, or by addition/deletion of one atom in the coordination sphere. Per donor atom to a single metal site, the ligand charge transfer order is peroxo ≥ oxo ≫ TACN > acetate. The TACN > acetate donation is expected from the spectrochemical series.[73,74] Replacement of a single nitrogen donor atom by a carboxylate oxygen should then give a weaker ligand field. (However, the strong charge transfer, metal−ligand

(74) Huheey, J. E., *Inorganic Chemistry*, 2nd ed.; Harper and Row International Edition: New York, 1979.

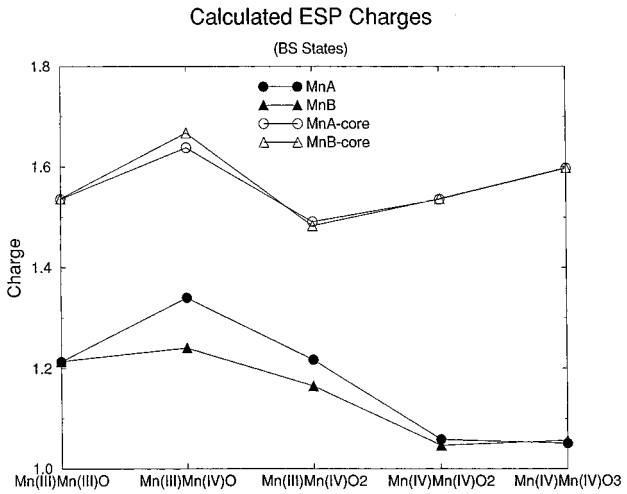

Figure 6. Calculated ESP charges (in $|e|$) on Mn ions for full and core-only systems. Note only BS states were plotted since HS states give almost identical results.

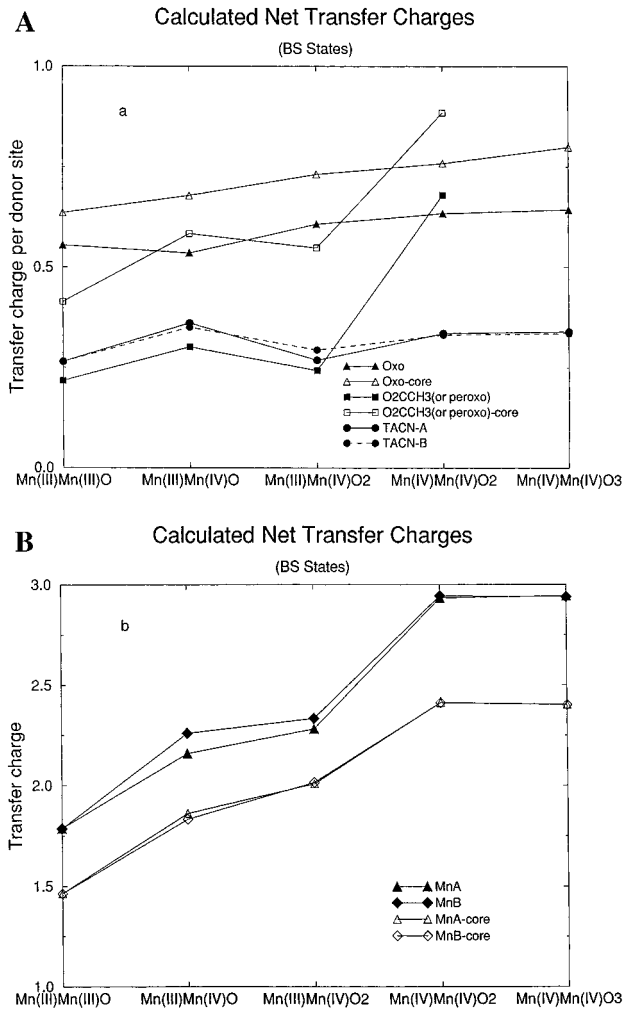

Figure 7. Transfer charges on different groups calculated from ESP charges with formal group charges as the reference states (charge transfer per donor atom to each Mn site for ligand groups): (a) ligands; (b) Mn ions.

bonding, and metal−ligand covalency of the peroxo and oxo ligands does not allow a simple correlation with the spectrochemical ligand series since the latter is related only to the ligand effect on the energies of nonbonding and/or antibonding d → d transitions.) The complete TACN ligand is a strong donor, donating about 1e$^-$ to the adjacent metal site. In the absence of the TACN ligands, the donation from all remaining ligands increases dramatically, so that there is strong charge compensation from the other ligands to make up for the absence of TACN. Despite this, the Mn charges are much higher in the core-only complexes and increase overall with the oxidation state and the number of oxo ligands.

3.5. Charges and Spin Densities in the Mn^{IV}_2−Peroxo Complex. From the work of Bossek *et al.*,[25] complex **4** is known to eliminate molecular oxygen from the formally $Mn^{IV}_2(\mu\text{-}O)_2(O_2^{2-})(TACN)_2$ system. The resulting Mn^{III}_2 complex has not been isolated, but rather undergoes a series of complicated disproportionation reactions which are not well understood. In this context, we briefly examine the charges and spin densities on the peroxo and μ-oxo atoms for both the broken symmetry and high spin states. The charge distributions are very similar for both the HS and BS states, so we need to focus only on the common features here. Each peroxo oxygen atom (O_p) has a calculated ESP charge of −0.32, which is considerably less than that for a μ-O atom, −0.73. Clearly, the O_p atoms are closer to neutral oxygen. In addition, the net manganese ESP charges are quite low, consistent with elimination of neutral O_2, and the electrostatic attraction between Mn and O_p will be smaller than with μ-O. Figure 7a shows that each O_p donates far more charge to the metal than the corresponding acetate oxygen in the most closely related complex **3**, $Mn^{III}Mn^{IV}(\mu\text{-}O)_2(OAc)_2(TACN)_2$, and the acetate O charge is much more negative, −0.63. The peroxo ligand strongly donates to the metal and does so preferentially to other ligands.

The spin densities show a significant difference between HS and BS. While in BS, the O_p spin density is only about 0.01 unpaired e$^-$, in the HS form this increases to +0.16 unpaired e$^-$, and these spins are parallel aligned to the Mn site spins. This also implies that in the high-spin state, the peroxo ligand is donating minority spin density to the Mn sites, which is largely bonding density. The minority spin density on Mn in HS is large, 1.61 β spin electrons, and this is only slightly less than that found in the BS state. While the net spin population on peroxo is substantial, this is still different from the 1 unpaired e$^-$ per oxygen atom in the ground state of O_2, where $S = 1$, but the HS state with spin $S = 3$ is possibly on the reaction pathway. The HS state lies rather low in energy, being only $-12J$, or about 4 kcal/mol above the ground $S = 0$ state from the experimental results (while from the calculations, E(HS) − E(S = 0) is 8 kcal/mol.) Such an energy is thermally accessible and may provide a point along the pathway to products. It is likely that the higher peroxo spin density in the HS state contributes to an energy lowering relative to E(BS) or E(S = 0), since triplet molecular oxygen is considerably lower in energy than singlet oxygen. There is a relative minimum in E(HS) − E(BS) at Mn^{IV}_2−peroxo in Figure 4. A further two-electron excitation from minority → majority spin would yield an $S = 5$ state which would then correspond in spin to the parallel coupled dissociation product of triplet oxygen ($S = 1$) with high-spin Mn^{III}_2 ($S = 4$). The possible vector couplings of Mn^{III}_2 ($S = 4$) with O_2 ($S = 1$) yield total spin $S_t = 3, 4, 5$. Examination of the energy level diagram, Figure 8, and the HOMO of the HS, Figure 9, $S = 3$ complex indicates another possible intermediate of lower net spin, possibly at low energy. A two-electron excitation from majority spin → minority spin, for example from $42A'\alpha 32A''\alpha \rightarrow 40A'\beta 41A'\beta$ will yield a net spin $S = 1$ for the complex, composed approximately from a triplet O_2 moiety, $S_{O_2} = 1$ antiferromagnetically coupled to a $S_{Mn^{III}_2} = 2$. This would imply that each Mn(III) site is effectively $S = 1$, intermediate spin. With elimination of molecular oxygen,

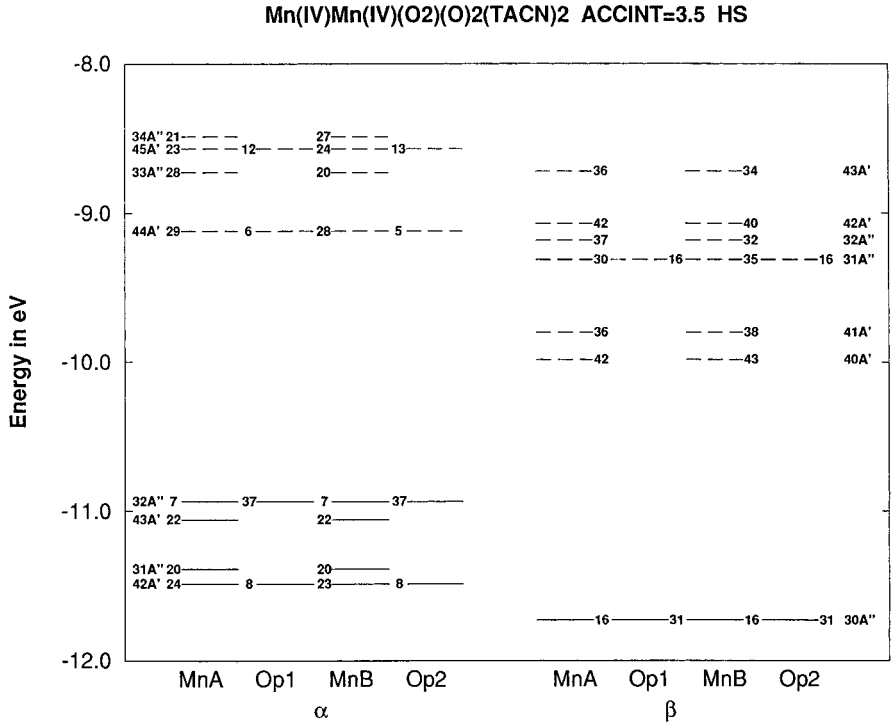

Figure 8. Orbital energy levels and MO composition high spin Mn^{IV}_2−peroxo TACN complex. Occupied levels are shown as solid lines, and empty levels, as dashed lines.

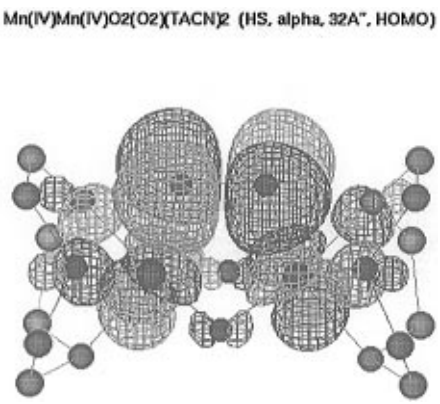

Figure 9. Isovalue surface of the highest occupied molecular orbital (HOMO) of the high spin $S = 3$ for Mn^{IV}_2−peroxo TACN complex.

the Mn^{III}_2 product would be smaller than the original complex, so stronger coordination to the product by the counterion/solvent environment probably also contributes to lowering the barrier for O_2 dissociation. Further, the peroxide ligand has an O−O bond distance of 1.46 Å in complex **4**, near that of free peroxide, while triplet molecular oxygen has a much shorter bond length of 1.21 Å. O_2 elimination then may involve a concerted O−O bond shortening with coupled charge transfer to the Mn sites. Such a bond compression should lower the gap between the high-lying α and low-lying β spin orbitals shown in Figure 8 for the high-spin $S = 3$ complex, although there will also be an energy cost to this process. Consistent with this proposal, The HOMO 32A″α in Figure 9 shows very substantial peroxide π^* character, and the LUMO 40A′β shows mainly Mn(d) character. The energetics of these spin states are currently under investigation.

3.6. Energy Level Structures. Figures 10−12 show energy level structures of the broken symmetry state for complexes **1**−**3**. The high lying occupied and important empty levels are shown. The extensive metal−ligand covalency in the high-lying occupied levels is evident from the total metal percentage

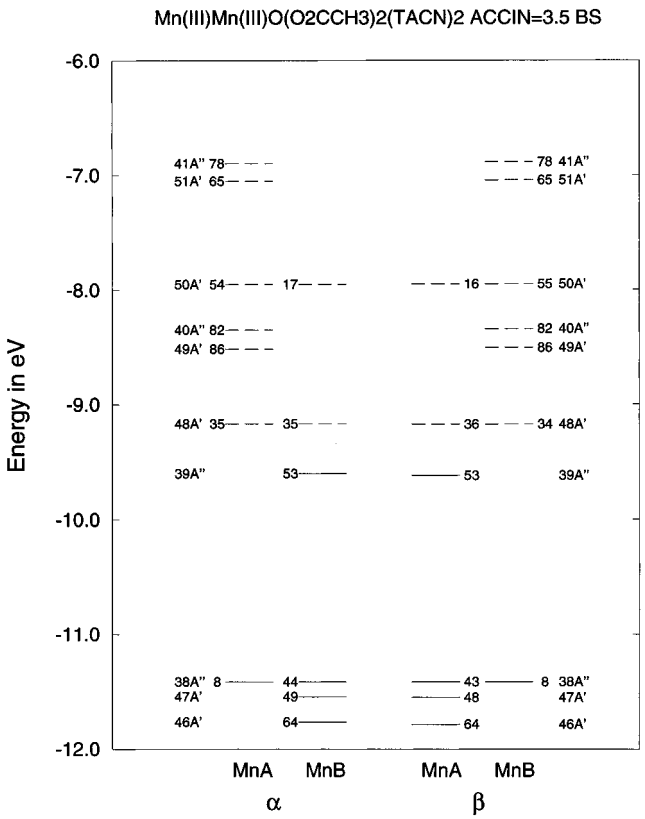

Figure 10. Broken symmetry energy level diagram and MO composition on Mn for Mn^{III}_2, of complex **1**.

in these levels. In fact, the metal character is spread over a wide range of energies in the occupied orbital set. In previous work, we have called this the "mixed-level scheme" to indicate the high metal−ligand covalency.[75] This type of energy level structure is distinct from the "normal-level scheme" where all the occupied mainly metal levels lie above all the mainly ligand levels, and from the "inverted-level scheme" (found in FeS complexes), where occupied mainly ligand levels lie above the

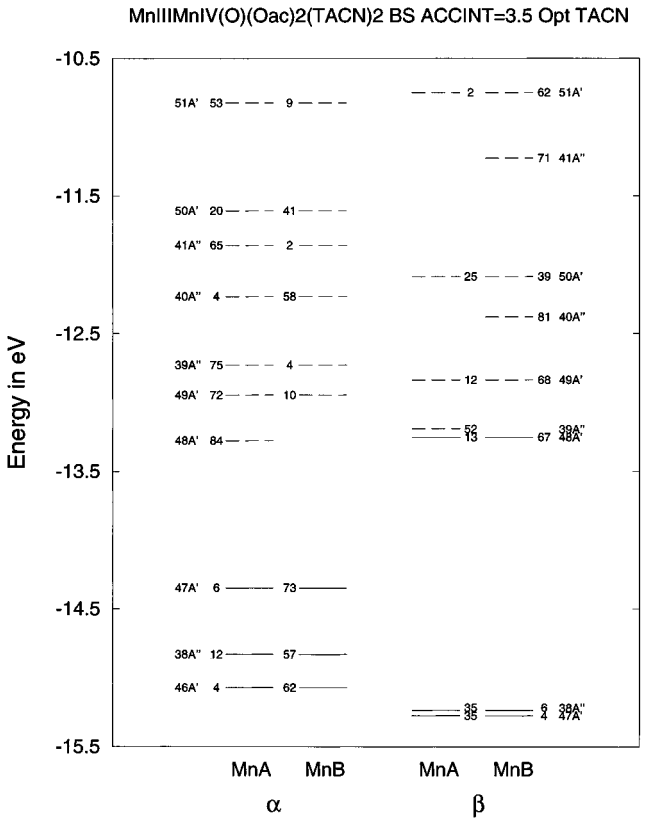

Figure 11. Broken symmetry energy level diagram and MO composition on Mn for $Mn^{III}Mn^{IV}$, of complex **2**.

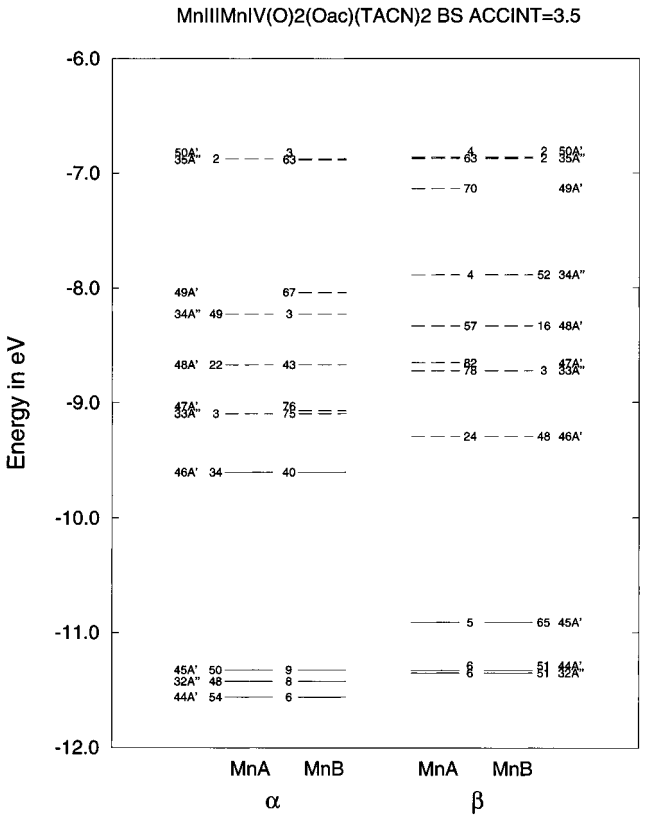

Figure 12. Broken symmetry energy level diagram and MO composition on Mn for $Mn^{III}Mn^{IV}$, of complex **3**.

occupied majority spin metal levels, and below mainly empty minority spin levels. The highest occupied orbital of complex **1** is 39A″ and α and β spin orbitals are energetically degenerate, but spatially distinct (on the left or right of the molecule). This orbital shows a strong antibonding interaction of Mn(d_{yz}) with acetate O(p) and TACN N(p), and there is little interaction across the acetate bridge to the alternate Mn. On oxidation to complex **2**, one electron is removed from this orbital, from 39A″ α. Surprisingly, when this occurs, there is a rearrangement of occupied β orbitals so that the previously empty 48A′ β becomes filled and 39A″ β becomes empty (state: $(39A'' \beta)^0(48A' \beta)^1$), comparing Figure 10 with Figure 11. This electron rearrangement also corresponds to a change in the spin-coupling scheme. For complex **1**, $S_1 = S_2 = 2$ and $S = 0$ while for the complex **2** ground state $S_1 = 1$, $S_2 = {}^3/_2$, and $S = {}^1/_2$.

The ordinary aufbau state with occupancy $(39A'' \beta)^1(48A' \beta)^0$ has a total BS energy only 0.34 eV higher than the complex **2** ground BS state. (Correspondingly, the coupling scheme of the aufbau state is closer to that in complex **1** with $S_1 = 2$, $S_2 = {}^3/_2$, and $S = {}^1/_2$.) Pseudo-Jahn−Teller mixing of these two nearly degenerate orbitals can occur with geometric distortion from $C_s \rightarrow C_1$ (no symmetry), and this is consistent with the distorted geometry seen experimentally. As previously mentioned, the two spin ladders of the aufbau and nonaufbau states can interact via pseudo-Jahn−Teller mixing.

Comparing the energy level structure for complex **2** to complex **3** (Figures 11 and 12), the ground state-to-excited state energy level splitting becomes much larger when one carboxylate is replaced by an oxo ligand. The HOMO of complex **3** is 46A′α, which shows considerably more interaction between the "formally" Mn(III) and Mn(IV) sites than either the HOMO or LUMO of complex **2**. These three orbitals are depicted in isovalue contour maps in Figure 13a−c. The HOMO 39A′ of the $Mn^{IV}_2O_3$ complex **5** shows strong oxo → metal bonding character (see Figure 13d). This is consistent with the strong AF coupling calculated and observed in this system, and the HOMO−LUMO gap increases compared with all other complexes **1**−**4**.

3.7. Effective Ligand Field Diagrams. The position of the ligand field levels is often used to describe the active site electronic structures of transition metal complexes. However, in the presence of extensive metal−ligand covalency, as shown in Figures 8 and 10−12, comparing the ligand field levels of different complexes and oxidation states becomes a difficult task because metal character is spread over a wide energy range. Exchange coupling between the transition metal sites further complicates these issues. We have approached this problem by constructing an "effective" ligand field picture. Basically, a Mulliken population weighted average is calculated for each Mn(d) component, and this is done separately for each Mn atom and spin index. We use a different procedure for majority spin and minority spin metal levels, which reflects their different roles. For majority spin Mn(d) levels, there is some Mn character in deep lying metal−ligand bonding orbitals; above this lies the occupied nonbonding and antibonding metal region, and finally, some majority spin levels with substantial metal character are unoccupied. Since ligand field theory ignores the deep lying bonding region, but essentially includes the other energy regions, both occupied and empty (above the Fermi level), we follow an analogous procedure for the effective ligand field energy weighting. We ignore levels below a percentage Mulliken threshold (less than 6% works well and consistently for different complexes), which filters out the deep lying bonding levels. Then a Mulliken weighted average is performed over both the occupied and unoccupied energy region. In contrast, the minority spin levels can be separated into two parts: the occupied energy region and the empty region (above

(75) Noodleman, L.; Peng, C. Y.; Case, D. A.; Mouesca, J.-M. *Coord. Chem. Rev.* **1995**, *144*, 199−244.

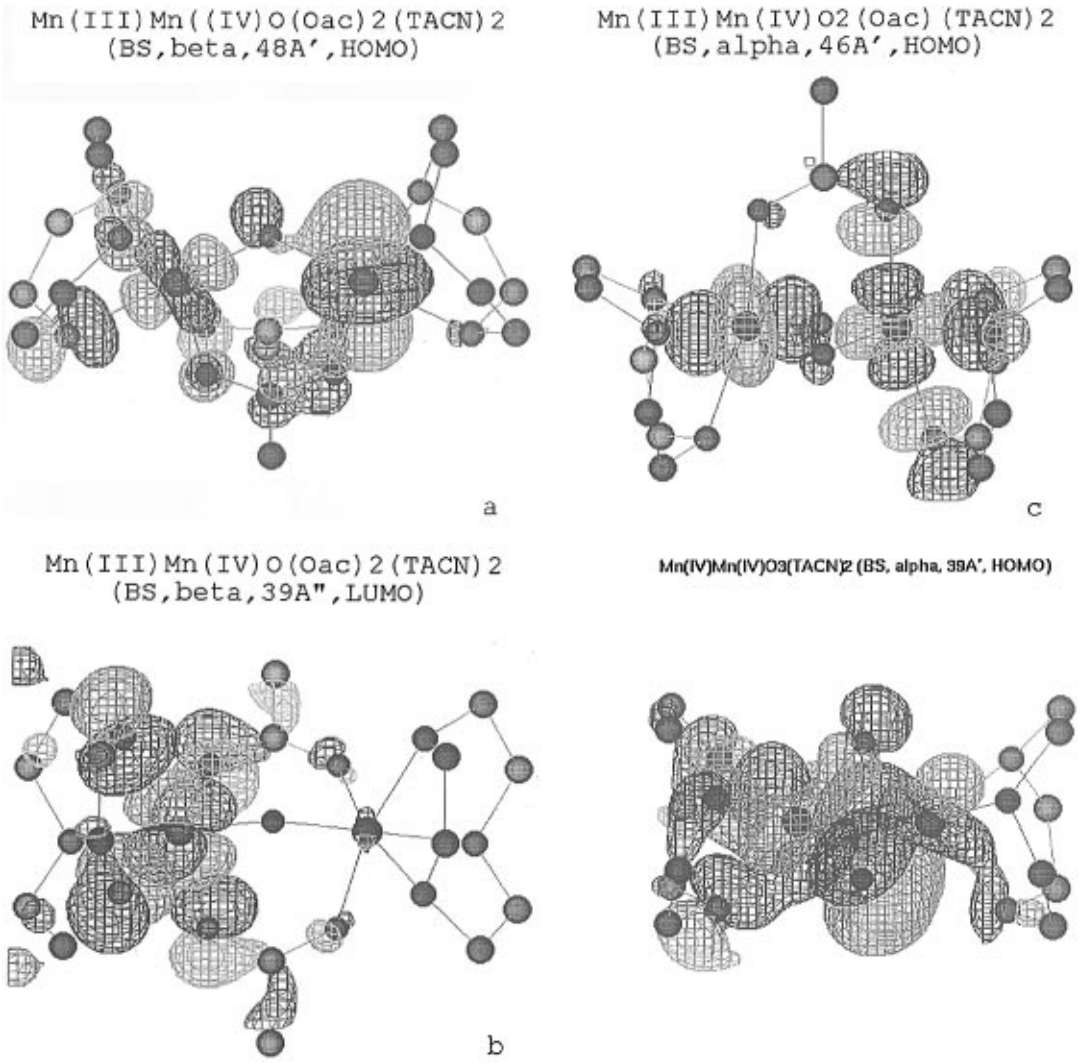

Figure 13. Orbital isovalue surface plots for high lying orbitals: (a) HOMO of BS state for complex **2** ($Mn^{III}Mn^{IV}$−oxo); (b) same as part a but for LUMO; (c) HOMO of BS state for complex **3**; (d) HOMO of BS state of complex **5** ($Mn^{IV}{}_2O_3$), 39A′ α spin orbital nearly degenerate with occupied 39A′ β.

the Fermi level). Minority spin orbitals above the Fermi level correspond to the nonbonding and antibonding d states of ligand field theory; in contrast, the occupied minority spin Mn (d) contributions correspond to ligand → metal back-bonding and polarization/charge transfer and have no equivalent in ligand field theory. Weighted averages were done separately on these two sets of minority spin orbitals, and no percentage threshold was used. We report these ligand field levels, and the corresponding percentage Mulliken populations for complexes **1**−**3** in Figures 14−16. (For the majority spin, the reported Mulliken populations include the unoccupied orbitals. As a consequence of this, Figures 14−16 cannot be used to assess which majority spin d components are mainly filled or empty. Instead, all Mn(d) components have some fractional occupation. A more global analysis of total Mn(d) populations is provided in Tables 5 and 6 and Figure 5.) The minority spin polarization/charge transfer levels are also included in the diagrams, and, as expected, show lower populations than the ligand field levels. Comparable diagrams for the core-only complexes, Figures S1−S3 are included in the Supporting Information.

Figures 14−16 show the patterns of spin-polarized ligand fields. There is both a spin polarization splitting between majority spin and minority spin on each metal site, and a smaller ligand field splitting of the different d orbitals. For complexes **1**, **2** the highest lying orbitals are Mn (d_{yz}) and (d_{xy}), corresponding to e_g of the approximate octahedral field. Mn(d_{xy}) interacts most strongly with the μ-O bridge, as well as with one nitrogen from TACN, while Mn(d_{yz}) interacts with the TACN Nσ donors, and with acetate O(pσ). Mn($d_{x^2-y^2}$, d_{z^2}, d_{xz}) form the t_{2g} set. The spin-polarization pattern for the broken-symmetry state is also apparent for the equal valence $Mn^{III}{}_2$ state where the β spin levels for Mn(A) are energetically the same as the α spin for Mn(B), and where α spin on Mn(A) is the same as β spin on Mn(B). When one electron is removed to obtain the mixed-valence $Mn^{III}Mn^{IV}$ complex, Figure 15, the two sites become inequivalent. In complex **2**, the Mn(B) site shows a much smaller spin polarization splitting than Mn(A), because of the smaller net spin population on Mn(B). (Here, we compare the splitting between Mn(A) β (majority spin, occupied) and Mn(A) α (minority spin, empty), which is much larger than the corresponding splitting between Mn(B) α and Mn(B) β.) Mn(A) corresponds to the spin $S_2 = {}^3/_2$ site and Mn(B) to the $S_1 = 1$ site as seen in Table 5A. Still, the pattern of the ligand field splitting for a given Mn site and spin index is similar to that in $Mn^{III}{}_2$. However, the spin-polarization splitting for the formally $Mn^{III}{}_2$ complex **1** is larger than for the $Mn^{III}Mn^{IV}$ complex **2**, consistent with the larger net site spins of the former system. The occupied minority spin levels show a splitting pattern opposite to that for the unoccupied minority spin levels, indicative of metal−ligand bonding in the former. For complex **3**, Figure 16, the highest lying ligand field levels are Mn(d_{xz},$d_{x^2-y^2}$) of the e_g set with d_{xz} highest, reflecting

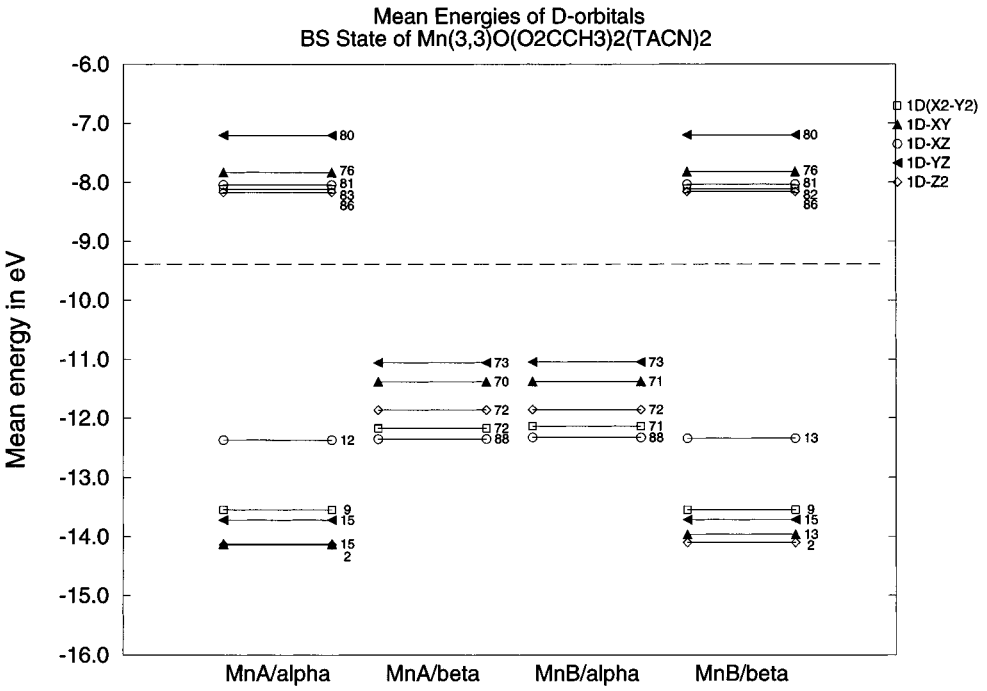

Figure 14. Effective ligand field energy (mean orbital energies weighted by Mulliken populations) diagram of complex **1** for the BS state. This shows the ligand field and spin polarization splittings.

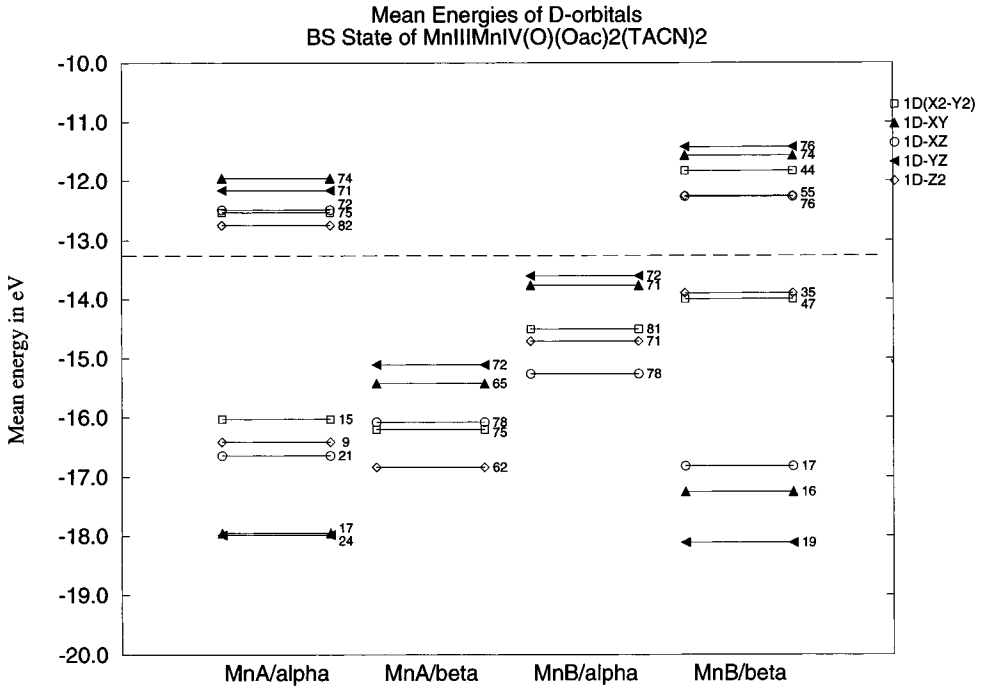

Figure 15. Effective ligand field diagram for complex **2**. See also Figure 14 for details.

the presence of $(\mu\text{-O})_2$ and one (OAc) ligand in place of one $(\mu\text{-O})$ and $(\text{OAc})_2$. This is consistent with experimentally based spectroscopic assignments from electronic absorption, magnetic circular dichroism (MCD), and resonance Raman enhancement profiles of ligand field levels in related $Mn^{III}Mn^{IV}(\mu\text{-O})_2$ complexes (noting that our *xz* plane is the $Mn_2(\mu\text{-O})_2$ plane which corresponds to the *xy* plane in the experimental paper, interchanging *z* and *y* axes).[4] The presence of $(\mu\text{-O})_2$ also leads to a larger splitting between the highest lying occupied and the lowest empty orbitals in complex **3** compared to complex **2**. In complex **3**, Mn(A) corresponds to the spin $S_2 = {}^3/_2$ site, and Mn(B) to the $S_1 = 1$ site (Table 5A). Figures S1−S3 for the core-only calculations show a larger spin polarization splitting and a smaller splitting among d orbitals for the same site and spin index, consistent with the much weaker ligand fields here. Furthermore, the pattern of the d orbital splitting is different since the ligand field is now not even approximately octahedral. These two results are entirely consistent with the calculated ferromagnetic shift of the spin coupling for the core-only vs the complete complexes.

4. Conclusions

We have calculated the electronic structures of five different manganese−oxo dimer complexes using density functional methods combined with the broken symmetry/spin projection method.

Systems studied were $[Mn^{III}_2(\mu\text{-O})(OAc)_2(TACN)_2]^{2+}$ [56] (**1**), $[Mn^{III}Mn^{IV}(\mu\text{-O})(OAc)_2(TACN)_2]^{3+}$ [24] (**2**), $[Mn^{III}Mn^{IV}(\mu\text{-O})_2$-

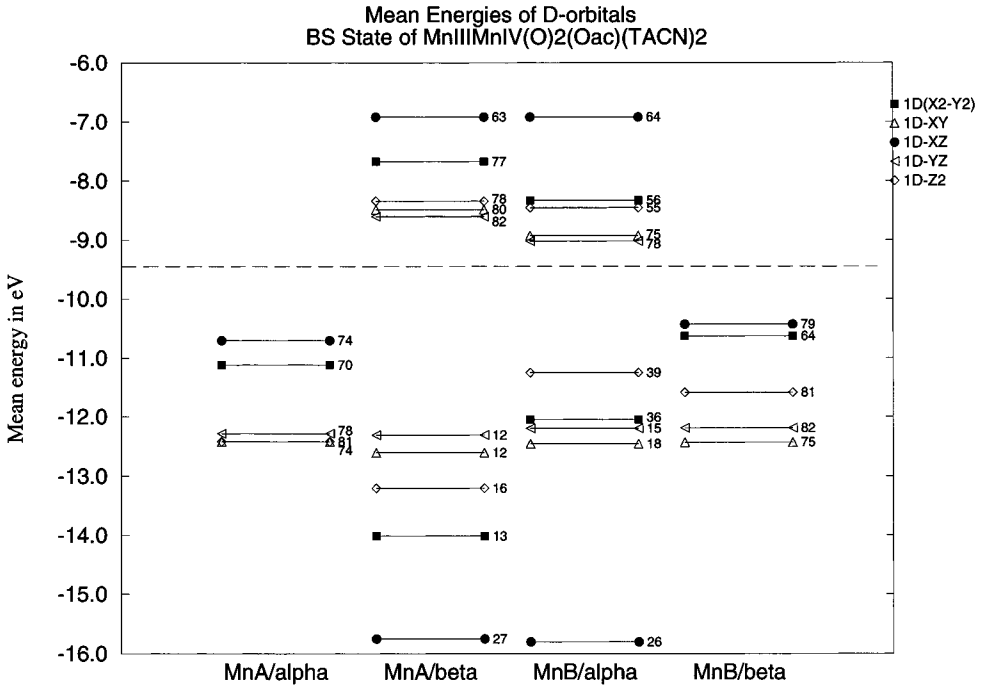

Figure 16. Effective ligand field diagram for complex **3**. See also Figure 14 for details.

$(OAc)(TACN)_2]^{2+}$ [22] (**3**), $[Mn^{IV})_2(\mu\text{-}O)_2(\mu\text{-}O_2{}^{2-})(TACN)_2]^{2+}$ [25] (**4**), $[Mn^{IV}{}_2O_3(TACN)_2]^{2+}$ [38] (**5**). Despite the very small energy differences involved, there is a good correspondence between calculated and experimental Heisenberg J parameters. We have also examined the effects on the spin coupling parameter, J_{eff} in $Mn^{III}Mn^{IV}$ complexes when partial or complete delocalization due to the B parameter is taken into account. Surprisingly, in the mixed-valence systems, the intermediate spin $S = {}^5/_2$ state lies below $S = {}^7/_2$ in the two complexes examined. The energy differences from the calculations are a few tenths of an electronvolt, and two distinct spin ladders are expected for complex **2**, while there may be configuration mixing of the two spin ladders for complex **3**. This result is consistent with spin coupling between Mn with site spins $S_1 = 1$, $S_2 = {}^3/_2$, corresponding to intermediate spin Mn(I) and Mn(II), respectively, as depicted in Scheme 1, instead of the coupling expected from the formal oxidation states, $S_1 = 2$, $S_2 = {}^3/_2$ from high-spin Mn(III) and Mn(IV). The spin and charge distributions in the broken symmetry ground states are also consistent with intermediate spin $S_1 = 1$, $S_2 = {}^3/_2$.

In addition to the importance of strong exchange pathways via short Mn−Mn and Mn−oxo distances, the antiferromagnetic coupling strength usually increases with the increasing strength of the total ligand field, including the terminal ligands, and with higher formal Mn oxidation states. The only exception to these rules is for the formally $Mn^{IV}{}_2$−peroxo complex, where the strong metal−peroxo covalency, and the fact that the ground state of molecular oxygen O_2 is a triplet ($S = 1$), probably lowers the energy of the excited high-spin state $S = 3$, and other states with $S \geq 1$.

In previous work, we have calculated the magnetic exchange interactions in the cubane complex, $[Mn^{IV}Mn^{III}{}_3O_3Cl_7(O_2CCH_3)_3]^{3-}$.[66] Weaker J coupling parameters were found both from the calculations (using a comparable VWN−Stoll[42,76,77] potential plus Becke[43,44] exchange energy correction) and experimentally compared with those in complex **3**. This result is consistent with the more extensive chloride and carboxylate coordination in the cubane complex, since chloride and carboxylate oxygen are weaker field ligands than TACN nitrogen. Also notable in the cubane complex is the result that the formal Mn(III) sites definitely have spin $S_i = 2$ (see Table 3 and Figure 5[66] for relevant energy gaps between occupied and empty Mn(III) levels), antiferromagnetically coupled to a formal Mn(IV) site $S_i = {}^3/_2$ to give $S = {}^9/_2$ as found experimentally. Such a Mn(III) spin change from $S_i = 1$ to 2 is sensible given the weaker site ligand field in the cubane. In this cubane system as well as in the dimers studied, the d electron count does not correspond to that expected for formal Mn(IV) and Mn(III) sites; instead, there are higher populations of both dα and dβ electrons. So far, optical spectra in $Mn^{III}Mn^{IV}O_2$ dimer complexes,[4] and ^{55}Mn EPR hyperfine tensors[78] have been interpreted within the context of formal Mn(III) and Mn(IV) d orbital occupancies, although substantial effects of metal−ligand covalency were noted. In future work, it would be valuable to test the more complicated Mn d orbital occupancies we have found in relation to both optical and EPR hyperfine properties. In this context, we also note the recent density functional work of Ghosh et al. on $Fe^{IV}Fe^{III}(\mu\text{-}O)_2$[79,80] and $Fe^{IV}O$(porphyrin) complexes. Fe(IV) is formally isoelectronic to Mn(III) and often has spin $S = 1$, particularly in the form $(FeO)^{2+}$, and formally in the delocalized $Fe^{IV}Fe^{III}(\mu\text{-}O)_2$ complex, since $S_1 = 1$ coupled to $S_2 = {}^1/_2$ yields the observed $S = {}^3/_2$ ground state. Here, Ghosh et al.[79] find that the total d electron count strongly exceeds the formal d count from $Fe^{IV}Fe^{III}$, while the Fe spin populations are less than the formal $Fe^{IV}(O^{2-})_2Fe^{III}$ would indicate.

The calculated charge distributions in the Mn−O dimers show strong metal−ligand covalency. In fact, as the formal oxidation states of the Mn sites increase, the net Mn charges generally show a slow decrease, consistent with very strong ligand →

(76) Stoll, H.; Pavlidou, C. M. E.; Preuss, H. *Theor. Chim. Acta* **1978**, *149*, 143−149.
(77) Stoll, H.; Golka, E.; Preuss, H. *Theor. Chim. Acta* **1980**, *55*, 29−41.
(78) Zheng, M.; Khangulov, S. V.; Dismukes, G. C.; Barynin, V. V. *Inorg. Chem.* **1994**, *33*, 382−387.
(79) Ghosh, A.; Almlof, J.; Que, L., Jr. *Angew. Chem., Int. Ed. Engl.* **1996**, *35*, 770−772.
(80) Ghosh, A.; Amlöf, J.; Que, L., Jr. *J. Phys. Chem.* **1994**, *98*, 5576−5579.

metal charge transfer, particularly from μ-oxo or μ-peroxo ligands. TACN is a better donor ligand than carboxylate, even when calculated on a per donor atom basis. The ligand atom charge transfer order is peroxo ≥ oxo ≫ TACN > acetate. In the $Mn^{IV}(\mu\text{-}O)_2(\mu\text{-}O_2)(TACN)_2$, each peroxo oxygen has a small charge (−0.32), much less than found for each μ-O atom (−0.73). The high spin $S = 3$ state lies quite low in energy, 8 kcal/mol from our calculations and about 4 kcal/mol based on the experimental Heisenberg spin coupling parameters. Potential molecular oxygen dissociation pathways involving a spin $S = 1$ state are described. Effective ligand field diagrams are constructed from the calculated energy levels which display the competition between spin-polarization splitting and the ligand field $t_{2g}-e_g$ splitting, and allow comparisons of electronic structure among different complexes.

Acknowledgment. We are grateful for funding of this work by NIH Grant GM43278 to L.N. at Scripps and Grant HL 13652 (D.N.H.). We thank E. J. Baerends and his group for use of the ADF codes and Scripps for computer facilities.

Supporting Information Available: Figures showing effective ligand field energy diagrams for BS state of the "core only" complexes (Figures S1−S3; Figure S1 is for complex 1, Figure S2 for complex 2, and Figure S3 for complex 3), energy differences between high spin and broken symmetry states and related experimental results (derived from J parameters) (Figures S4 and S5; Figure S4 is for high spin state $S = {}^5/_2$ and Figure S5 for $S = {}^7/_2$), and energy level diagrams and MO compositions of manganese ions and bridging ligands for various states of the TACN complexes **1**−**5** (Figures S6−S17), and tables of basis sets and fit functions used in the calculations (Table S1), Cartesian coordinates and Mulliken and ESP charges as well as spin populations for all complexes (Tables S2−S21), calculated molecular orbital energy levels with percentage contributions from metal ions and ligands (Tables S22−S27) and excitation energies for high spin $S = 3 \rightarrow S = 2$ transitions from Slater transition state calculations for complex **5** (Table S32) (186 pages). See any current masthead page for ordering information and Internet access instructions.

IC9514307